Inorganic Chemistry

Article

pubs.acs.org/IC

Experimental and Time-Dependent Density Functional Theory Characterization of the UV−Visible Spectra of Monomeric and μ-Oxo Dimeric Ferriprotoporphyrin IX

David Kuter,[†,‡] Gerhard A. Venter,[†,‡] Kevin J. Naidoo,[†,‡] and Timothy J. Egan*[,†]

[†]Department of Chemistry and [‡]Scientific Computing Research Unit, Department of Chemistry, University of Cape Town, Private Bag, Rondebosch 7701 South Africa

Supporting Information

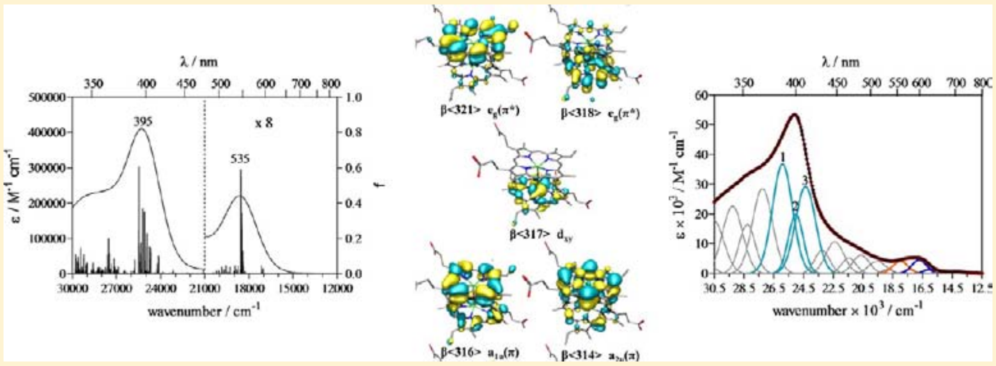

ABSTRACT: Speciation of ferriprotoporphyrin IX, Fe(III)PPIX, in aqueous solution is complex. Despite the use of its characteristic spectroscopic features for identification, the theoretical basis of the unique UV−visible absorbance spectrum of μ-[Fe(III)PPIX]$_2$O has not been explored. To investigate this and to establish a structural and spectroscopic model for Fe(III)PPIX species, density functional theory (DFT) calculations were undertaken for H_2O−Fe(III)PPIX and μ-[Fe(III)PPIX]$_2$O. The models agreed with related Fe(III)porphyrin crystal structures and reproduced vibrational spectra well. The UV−visible absorbance spectra of H_2O−Fe(III)PPIX and μ-[Fe(III)PPIX]$_2$O were calculated using time-dependent DFT and reproduced major features of the experimental spectra of both. Transitions contributing to calculated excitations have been identified. The features of the electronic spectrum calculated for μ-[Fe(III)PPIX]$_2$O were attributed to delocalization of electron density between the two porphyrin rings of the dimer, the weaker ligand field of the axial ligand, and antiferromagnetic coupling of the Fe(III) centers. Room temperature magnetic circular dichroism (MCD) spectra have been recorded and are shown to be useful in distinguishing between these two Fe(III)PPIX species. Bands underlying major spectroscopic features were identified through simultaneous deconvolution of UV−visible and MCD spectra. Computed UV−visible spectra were compared to deconvoluted spectra. Interpretation of the prominent bands of H_2O−Fe(III)PPIX largely conforms to previous literature. Owing to the weak paramagnetism of μ-[Fe(III)PPIX]$_2$O at room temperature and the larger number of underlying excitations, interpretation of its experimental UV−visible spectrum was necessarily tentative. Nonetheless, comparison with the calculated spectra of antiferromagnetically coupled and paramagnetic forms of the μ-oxo dimer of Fe(III)porphine suggested that the composition of the Soret band involves a mixture of $\pi \rightarrow \pi^*$ and $\pi \rightarrow d_\pi$ charge transfer transitions. The Q-band and charge transfer bands appear to amalgamate into a mixed low energy envelope consisting of excitations with heavily admixed $\pi \rightarrow \pi^*$ and charge transfer transitions.

INTRODUCTION

Recently there has been a revival of interest in the aqueous solution chemistry of free ferriprotoporphyrin IX [Fe(III)PPIX; ferriheme]. This arises from its implication in heme acquisition by both mammalian and bacterial cells[1−5] and more especially heme detoxification in the malaria parasite and in other blood-feeding organisms.[6−8] For many years it was assumed that Fe(III)PPIX spontaneously forms a μ-oxo dimer, μ-[Fe(III)-PPIX]$_2$O, as the dominant species in aqueous solution.[9] However, over the last 5 years three studies have clearly demonstrated that this is not the case.[10−12] Rather, in pure aqueous solution, it exists as a π−π dimer of H_2O−, HO−Fe(III)PPIX or a dimer comprising one of each species, depending on pH.[10] On the other hand, μ-[Fe(III)PPIX]$_2$O can be induced by addition of water-miscible aprotic solvents such as DMSO or acetone to high pH aqueous solutions of Fe(III)PPIX or by high salt concentrations.[11] Some authors

Received: May 31, 2012
Published: September 10, 2012

have provided evidence that certain antimalarials such as chloroquine can induce μ-[Fe(III)PPIX]$_2$O formation and detergents have also been shown to induce its formation.[13,14] Thus, the μ-[Fe(III)PPIX]$_2$O species remains of interest.

Several physical methods have been used to characterize μ-[Fe(III)PPIX]$_2$O. In the solid state, infrared (IR) and Mössbauer spectroscopy as well as magnetic susceptibility measurements have been used.[15−17] The closely related methyl ester of this species has been isolated, its structure determined by single crystal X-ray diffraction, and their resonance Raman spectrum recorded.[18,19] In solution, it has been distinguished from monomer or π−π dimer species by several techniques, including ^{1}H NMR spectroscopy, magnetic susceptibility measurements, and UV−visible spectrophotometry.[10,11,13,14,20] The last of these is the most convenient to use for identification of μ-[Fe(III)PPIX]$_2$O in solution, because it is fast, requires only very low concentrations, does not make use of expensive deuterated solvents, and can be performed directly on the sample of interest.

The UV−visible spectrum of μ-[Fe(III)PPIX]$_2$O differs markedly from that of the monomeric species in the Soret band, Q-band, and charge transfer regions.[10,11,20] These empirical differences have been used to identify the species present in solution. To date, the UV−visible spectra of H_2O−Fe(III)PPIX and μ-[Fe(III)PPIX]$_2$O have not been calculated. In earlier studies, spectra of monomers were assigned on the basis of computations involving the simplified porphyrin core of porphine or other symmetrically substituted porphyrins such as octaethylporphine (OEP), tetraphenylporphine (TPP), and its complexes with Zn(II) and Fe(III).[21−27] Very recently, spectra have been calculated for a model of the camphor-bound cysteinate complex of Fe(III)PPIX found in the active site of cytochrome P450 (P450$_{\text{cam}}$) as well as for diamagnetic Zn(II)PPIX, Ga(III)PPIX, and its μ-propionato dimer.[28,29] The IR spectra have also not been directly calculated for the H_2O−Fe(III)PPIX and μ-[Fe(III)PPIX]$_2$O species.

Here we report the results of structural, vibrational, and UV−visible spectroscopic modeling of H_2O−Fe(III)PPIX and μ-[Fe(III)PPIX]$_2$O using density functional theory (DFT). We compare the structures to their Fe(III)porphine analogs and to reported crystal structures of related compounds. The computed IR and UV−visible spectra are compared to their experimental counterparts. Time-dependent DFT (TD-DFT) is shown to be able to model the spectra of H_2O−Fe(III)PPIX and μ-[Fe(III)PPIX]$_2$O remarkably well, reproducing the substantially different spectroscopic features observed experimentally. We report the use of room temperature magnetic circular dichroism (MCD) spectroscopy as a tool to distinguish between these species. The most important MCD and UV−visible spectroscopic envelope peaks have been deconvoluted and compared to the TD-DFT calculated spectra. This has permitted us to postulate reasons for the marked differences in the absorbance spectra of these two species.

■ EXPERIMENTAL SECTION

IR spectra were recorded using a Perkin-Elmer Spectrum 100 FT-IR spectrophotometer. All samples were dried in a desiccator over phosphorus pentoxide or by using a ThemoSavant YOD 230 lyophilizer. H_2O−Fe(III)PPIX was obtained by dissolving hemin (Cl−Fe(III)PPIX, 150 mg, Fluka) in 10 mL of NaOH (0.1 M) and adding 1 M $HClO_4$ until a measured pH of 5.0 was obtained, producing a Fe(III)PPIX precipitate. The mixture was then centrifuged at 4000 rpm for 20 min, the supernatant discarded, and the remaining water removed by lyophilization. The IR spectrum of this precipitate confirmed that it was H_2O−Fe(III)PPIX and not Cl−Fe(III)PPIX (see Supporting Information, Figure S1). μ-[Fe(III)-PPIX]$_2$O was obtained by modifying the procedure of Silver and Lukas, where porcine hematin (20 mg, Sigma-Aldrich) was dissolved in 0.5 mL of HCl (1 M) and 20 mL of acetone.[17] To the resulting solution, NaOH (5 M) was slowly added until precipitation occurred. The supernatant was decanted and the precipitate dried in a desiccator.

All UV−visible spectra were recorded on a Varian Cary 100 UV−visible spectrophotometer, and MCD spectra were recorded at room temperature on a Chirascan-Plus CD spectrophotometer operating over the wavelength range 165−1100 nm with a MCD accessory calibrated at 0.977 T. The spectra of H_2O−Fe(III)PPIX (22 500−30 000 cm^{-1}) were obtained by adding 15 μL of a stock solution of hemin (1 mM in 0.1 M NaOH) to an aqueous acetone solution (5.64 M) and acidifying it with 100 μL of nitric acid (0.2 M), to give a final volume of 2 mL with a H_2O−Fe(III)PPIX concentration of 7.5 μM and a measured pH of 2. To record spectra of H_2O−Fe(III)PPIX between 12 500 and 22 500 cm^{-1}, the same procedure was followed with the exception that a more concentrated hemin stock solution was used (10 mM in 0.1 M NaOH). The spectra of μ-[Fe(III)PPIX]$_2$O between 12 500 and 30 000 cm^{-1} were obtained by diluting 15 μL of a hemin stock solution (1 mM in 0.1 M NaOH) in 40% (v/v) aqueous DMSO to give a final volume of 2 mL. MCD spectra were recorded using step scans with step size of 1 nm, bandwidth of 1 nm, and time per point of 0.5 s. In order to determine the spin state of H_2O−Fe(III)PPIX and to confirm formation of μ-[Fe(III)PPIX]$_2$O in solution, magnetic susceptibility measurements were conducted using the Evans NMR method on a Bruker Ultrashield 400 Plus NMR spectrometer (see Supporting Information S1).

Deconvolution of experimental absorbance spectra was facilitated by simultaneous fitting of the MCD spectra after correction for natural circular dichroism. In the case of the paramagnetic compounds used in this study, A-, B- and C-terms can be expected in the MCD spectra, with the latter expected to be dominant.[30] Since C-terms are temperature-dependent, they are more intense at low temperature, whereas A- and B-terms are essentially temperature-independent. A-terms arise in the case of degenerate excited states. For example, in the case of porphine, transitions from $a_{2u}(\pi)$- to $e_g(\pi^*)$-orbitals give rise to a doubly degenerate ^1E_u excited state, which would exhibit an A-type band in the MCD spectrum.[24,31] In the case of H_2O−Fe(III)PPIX and μ-[Fe(III)PPIX]$_2$O, the noncentrosymmetric structure lifts the degeneracy of the $e_g(\pi^*)$-orbitals. However, the resulting energy difference is very small, and so pseudo-A-type bands can be expected for the porphyrin Q- and B-bands. Such bands have a derivative shape. On the other hand, nondegenerate excited states exhibit B- and C-type bands, which have a Gaussian shape.[30] Deconvolution was achieved in the MCD spectra using the most parsimonious number of Gaussian functions to attain an acceptable fit, while simultaneously reproducing the absorbance envelope using identical wavelengths and line-widths.

■ COMPUTATIONAL DETAILS

All DFT calculations were performed using the Gaussian 09 software package.[32] Geometry optimizations and frequency calculations were performed using the OPBE generalized gradient approximation functional, which combines the optimized exchange OPTX functional of Handy and Cohen[33] with the PBE correlation functional of Perdew, Burke, and Ernzerhof.[34] This level of theory was used with the LANL2DZ basis set describing all atoms.[35−38] Fe(III)PPIX and porphine species were modeled without orbital symmetry constraints, and the use of a quadratically convergent self-consistent field (SCF) procedure was required to ensure convergence.[39] The starting geometries for H_2O−Fe(III)PPIX and H_2O−Fe(III)-porphine [H_2O−Fe(III)P] were obtained by modifying the β-hematin structure of Pagola et al.[40] The starting geometry of the μ-[Fe(III)PPIX]$_2$O and μ-oxo porphine species (μ-[Fe(III)P]$_2$O) was obtained by modifying the crystal structure of μ-oxo-bis[(protoporphyrin IX dimethyl ester)iron(III)].[18] In

Table 1. Computed (OPBE/LANL2DZ) and Experimental (italics) Bond Lengths (Å) and Angles (deg) of Fe(III)PPIX and Fe(III)P Species

	overall charge	Fe−O	$Fe-N_{por}$	Fe−O−Fe
H_2O−Fe(III)PPIX	−1[c]	2.276	2.077	NA
	0[d]	2.199	2.059	NA
	+1[e]	2.169	2.062	NA
H_2O−Fe(III)P	+1[f]	2.156	2.064	NA
CSD average H_2O−Fe(*III*)PPIX		*2.16(18)*	*2.00(4)*	*NA*
μ-$[Fe(III)PPIX]_2O$[a]	−4[g]	1.863	2.137	177.3
μ-$[Fe(III)PPIX]_2O$[b]	−4[g]	1.804	2.134	177.9
μ-$[Fe(III)P]_2O$[b]	0[h]	1.794	2.114	179.9
CSD average μ-$[Fe(\mathit{III})PPIX]_2O$		*1.76(1)*	*2.08(1)*	*176(3)*

[a] High spin ($S = {}^{10}/_2$). [b] Broken symmetry (antiferromagnetic coupling). [c] Fe (3+), porphyrin core (2−), 2 × propionate (1−) = −1. [d] Fe (3+), porphyrin core (2−), 1 × propionate (1−), 1 × propionic acid (0) = 0. [e] Fe (3+), porphyrin core (2−), 2 × propionic acid (0) = +1. [f] Fe (3+), porphyrin core (2−) = +1. [g] 2 × Fe (3+), 2 × porphyrin core (2−), 4 × propionate (1−), 1 × oxide ligand (2−) = −4. [h] 2 × Fe (3+), 2 × porphyrin core (2−), 1 × oxide ligand (2−) = 0.

the case of μ-$[Fe(III)PPIX]_2O$, the ester methyl groups were removed and one propionate side chain on the lower porphyrin was rotated to adopt a similar conformation to the other propionates in the molecule. Modifications to the crystal structures were made using the MOLDEN and Avogadro software packages.[41,42] Aqua species were modeled in the high spin state ($S = {}^5/_2$) while the antiferromagnetic coupling of the μ-oxo species was modeled using the method of broken symmetry described by Noodleman and co-workers.[43] Briefly, this involved a geometry optimization in the high spin ($S = {}^{10}/_2$) state, after which the electron spins on one Fe(III)-porphyrin were flipped and the geometry reoptimized using this new arrangement. Using the modified crystal structure coordinates as a starting geometry without first optimizing the structure in the high-spin ferromagnetic state failed to produce convergence of the antiferromagnetically coupled state. For the geometry-optimized structure of each species, the stability of the wave function was tested and frequencies were calculated to ensure a transition state or saddle point structure was not obtained.

Electronic spectra were calculated using the SMD solvent model by employing TD-DFT and the PBE0 functional using LANL2DZ to describe the iron atoms and LANL2DZdp, which includes diffuse and polarization functions, for all nonmetal atoms (PBE0/LANL2DZ:LANL2DZdp).[44−46] Calculated IR and UV−visible spectra were visualized using the GABEDIT and SWizard software packages.[47−49] Molecular orbital (MO) populations were analyzed using the Chemissian software package and visualized using GABEDIT with an electrostatic potential isosurface of 0.02 au. IR spectra were convoluted using Lorentzian functions at a half-width of 5 cm^{-1}, and UV−visible spectra were convoluted using Gaussian functions with half-widths of 685 and 1210 cm^{-1} for H_2O−Fe(III)PPIX and μ-$[Fe(III)PPIX]_2O$ respectively.

RESULTS

Structure. As a starting point for this investigation, we assessed various combinations of basis set and levels of theory to model the structure of H_2O−Fe(III)PPIX in a high spin ($S = {}^5/_2$) state, as found for this species in solution using magnetic susceptibility measurements (see Supporting Information, Table S1). Three functionals that were tested were BP86, M06, and OPBE.[33,34,50−52] These were used with the basis set LANL2DZ to describe all the atoms or with a combination of LANL2DZ describing iron and 6-31G(2d,p) describing all the other atoms. The BP86 functional was investigated because good agreement with experimental nuclear resonance vibrational spectra of Fe(III)OEP was recently reported by Scheidt and co-workers.[53] The M06 functional was assessed for its known capability to describe dispersion interactions.[52] Finally, OPBE was employed because Swart et al. showed that accurate spin energies and geometries can be obtained for iron systems with this functional.[54,55] In an effort to reduce the computational cost of these large systems, the effective core potential basis set, LANL2DZ, was employed, and results were compared with a model in which the larger 6-31G(2d,p) basis set that includes polarization functions was used to describe all non-Fe atoms.

Only the combination of the OPBE functional and LANL2DZ basis set (OPBE/LANL2DZ) was found to produce an acceptable geometry. With the BP86 functional, no convergence was obtained regardless of the basis sets used, despite employing strict quadratically convergent SCF criteria. Both the M06 and OPBE functionals produced unrealistic minimized structures after geometry optimization using the LANL2DZ and 6-31G(2d,p) basis set combination. In these structures the O−H bonds of the axial water ligand were orientated parallel to the plane of the porphyrin ring (see Supporting Information, Figure S2a). Using the M06 functional with only the LANL2DZ basis set resulted in a final structure in which a propionate side chain was reorientated to face the axial water ligand and a proton transfer from the axial water to the propionate group occurred (see Supporting Information, Figure S2b).

Having concluded that the OPBE/LANL2DZ combination was the most suitable for describing the structure of H_2O−Fe(III)PPIX in which the propionates are fully deprotonated, the same approach was used for the remaining species. These were H_2O−Fe(III)PPIX with either one or both propionate side chains protonated, μ-$[Fe(III)PPIX]_2O$ with fully deprotonated propionate groups, H_2O−Fe(III)P, and μ-$[Fe(III)P]_2O$. The antiferromagnetic coupling of the μ-oxo species was modeled using the method of broken symmetry. Selected bond lengths and angles of geometry optimized structures are listed in Table 1 and are compared to average values from the Cambridge Structural Database (CSD) for the aqua and μ-oxo species.[56] The Fe(III)−O bond length of H_2O−Fe(III)PPIX decreases substantially in going from the anionic to cationic species, which agrees most closely with the average experimental bond length. In general, the bond lengths and angles agree reasonably well with experiment (Table 1). The structures of H_2O−Fe(III)PPIX and μ-[Fe(III)PPIX]$_2$O are presented in Figure 1 and corresponding structures of H_2O−Fe(III)P and μ-[Fe(III)P]$_2$O are shown in the Supporting Information (Figure S3).

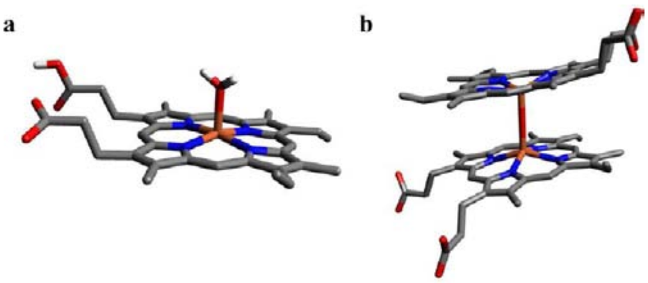

Figure 1. Geometry-optimized structures of Fe(III)PPIX species obtained with OPBE/LANL2DZ: (a) H_2O−Fe(III)PPIX and (b) μ-[Fe(III)PPIX]$_2$O. Porphyrin hydrogen atoms have been removed for clarity. Atom colors are red (O), blue (N), orange (Fe), gray (C), and white (H).

Vibrational Spectra. Calculated IR spectra were generated from the computed structures (Figure 2). Despite not using any scaling factors, good agreement between the calculated spectrum of the neutral H_2O−Fe(III)PPIX species and experiment is observed (Figure 2a,b). The computed IR spectrum of μ-[Fe(III)PPIX]$_2$O is dominated by the asymmetric Fe−O−Fe stretch at 724 cm^{-1} (Figure 2d). The peak assigned to this vibration is also very prominent in the experimental spectrum (Figure 2c); however, the frequency is considerably different (880 cm^{-1}). The other major peaks in the calculated spectrum coincide with a strong and very broad band centered at 1432 cm^{-1}. However, shoulders on this broad peak agree rather well with the frequencies of the calculated vibrations, although they are predicted to be less intense than observed (Figure 2e).

Although the assignment of the vibrational spectra of porphyrins, including Fe(III)PPIX, is well established, to our knowledge this is the first time that the spectra of H_2O−Fe(III)PPIX and μ-[Fe(III)PPIX]$_2$O have been calculated in full. Several IR features are worthy of mention. For the neutral species of H_2O−Fe(III)PPIX, there is one propionic acid group and one propionate. The ν(C═O) and ν(C−O) stretching frequencies of the acid side chain are calculated to occur at 1701 and 1102 cm^{-1} respectively, while that of the propionate side chain occurs at 1367 cm^{-1} (Figure 2b). For μ-[Fe(III)PPIX]$_2$O, in which all of the propionate groups are ionized, four peaks are obtained over the range 1496−1477 cm^{1} (Figure 2d). An interesting feature of the H_2O−Fe(III)PPIX spectrum is the H−O−H scissoring of the axial water ligand at 1606 cm^{-1} (Figure 2b, arrow), which has not previously been assigned in the experimental spectrum. A corresponding peak is prominent in the experimental spectrum of H_2O−Fe(III)PPIX but absent in that of Cl−Fe(III)PPIX (see Supporting Information, Figure S1a,b).

Calculated and Experimental Electronic Spectra. *H_2O−Fe(III)PPIX (S = $^5/_2$).* The molecular orbitals (MOs) associated with the major β-spin transitions calculated for H_2O−Fe(III)PPIX are shown in Figure 3, together with their corresponding MO diagram. While the α-spin MOs do contribute to $\pi \rightarrow \pi^*$ transitions, only the β-spin MOs are involved in ligand to metal charge transfer transitions, because this is a high-spin complex. Hence, in the interest of brevity, only the β-spin MOs are discussed. The results shown are for the model in which the axial Fe(III)−O bond length has been shortened to the experimental value reported for H_2O−Fe(III)OEP perchlorate (2.045 Å),[57] the most closely related compound for which a crystal structure has been obtained. A similar adjustment to the axial bond length in Cl−Fe(III)TPP was made in a recent study reported by Paulat and Lehnert.[24] No noteworthy difference in contributions to the MOs was observed compared to the model with an unaltered axial bond length (2.169 Å). Orbital contributions from the porphyrin, vinyl, and propionate groups and the iron atoms to the MOs shown in Figure 3 are presented in Table 2. All occupied

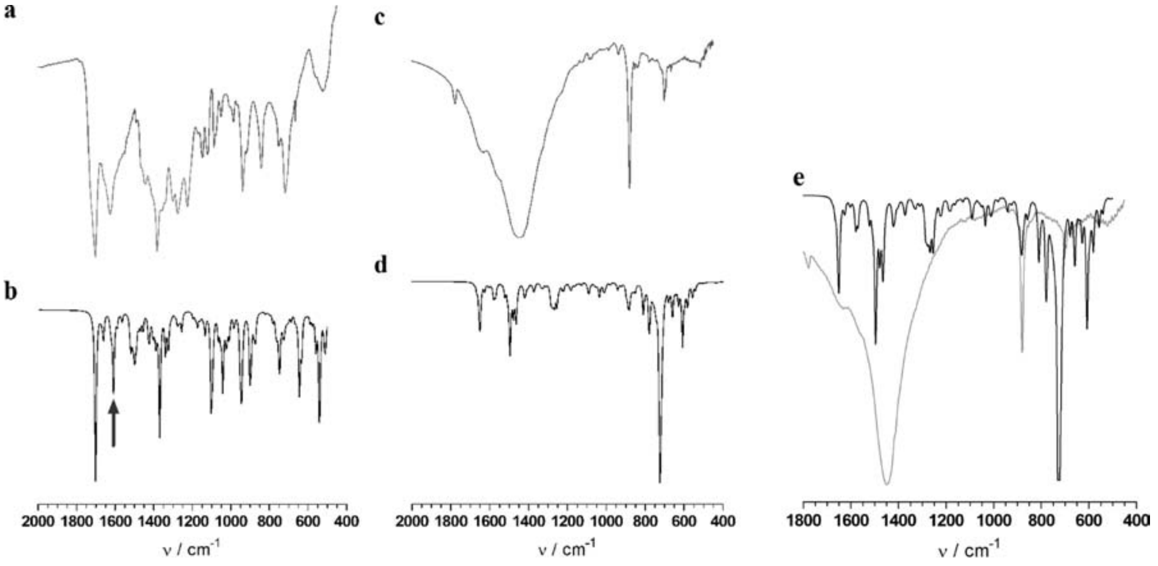

Figure 2. Calculated (black) and experimental (gray) IR spectra: (a) Fe(III)PPIX precipitated at pH 5, (b) H_2O−Fe(III)PPIX (neutral), (c) μ-[Fe(III)PPIX]$_2$O precipitated from aqueous acetone, and (d) μ-[Fe(III)PPIX]$_2$O. (e) y-Axis expansion of the computed IR spectrum of μ-[Fe(III)PPIX]$_2$O with the experimental spectrum overlaid. In spectrum b the peak arising from H−O−H scissoring is indicated with an arrow.

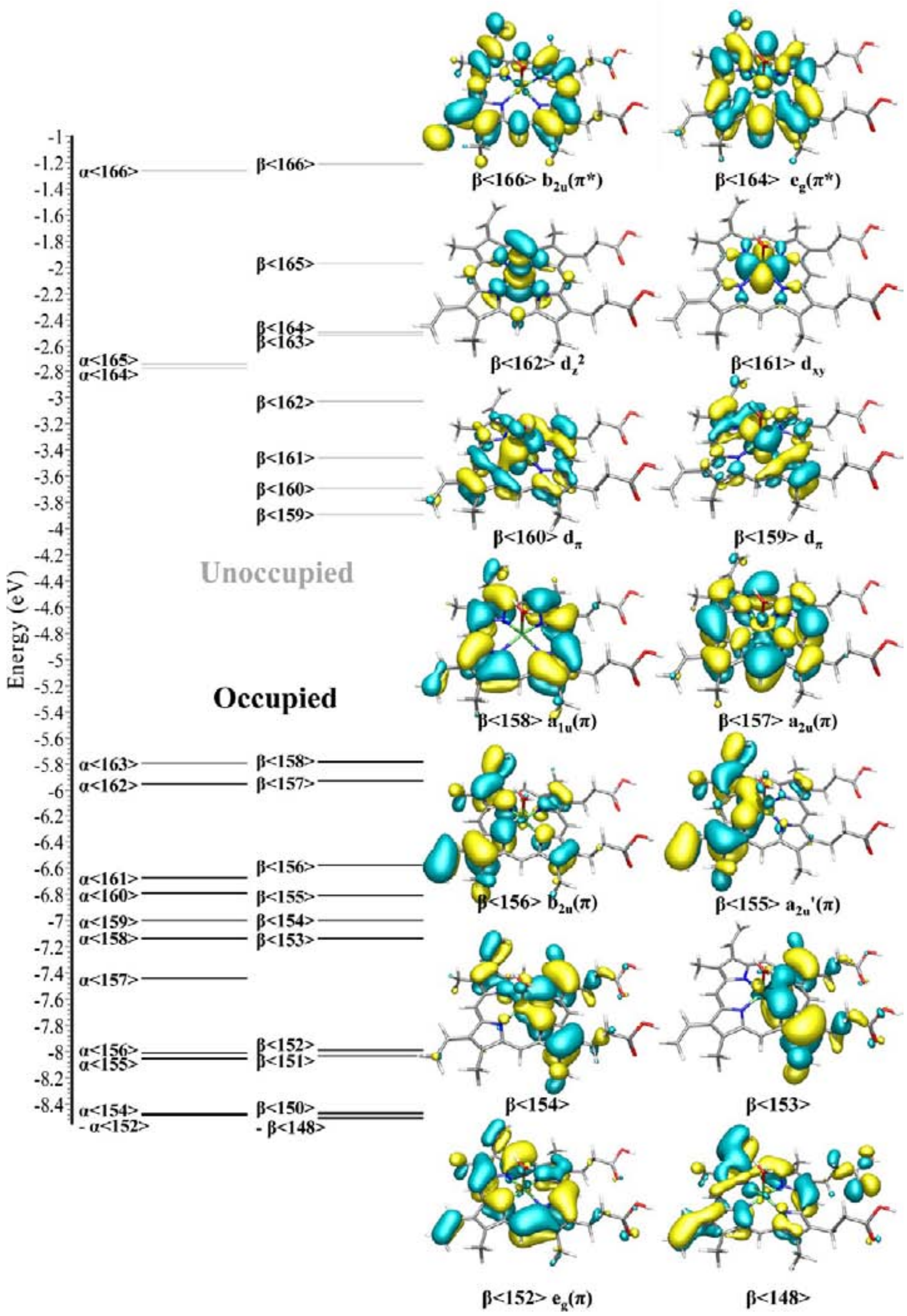

Figure 3. MO diagram of H_2O−Fe(III)PPIX showing selected β-spin MOs.

orbitals shown in Figure 3 are porphyrin π MOs. Two orbitals ($\beta\langle 155\rangle$ and $\beta\langle 156\rangle$) exhibit considerable vinyl character and two ($\beta\langle 149\rangle$ and $\beta\langle 150\rangle$) involve substantial contributions from the propionic acid groups. The unoccupied MOs $\beta\langle 159\rangle$ and $\beta\langle 160\rangle$ involve d_{xz} and d_{yz} iron atomic orbital contributions but also have large porphyrin π-orbital contributions (see Table 2) and are referred to from here on as d_π. By contrast, $\beta\langle 161\rangle$ has the smallest porphyrin contribution and a large contribution from the iron d_{xy}-orbital. Interestingly, $\beta\langle 162\rangle$ with d_{z^2} character has very little contribution from the axial ligand but also exhibits substantial porphyrin character, mostly on the N atoms. The unoccupied orbital with the most $d_{x^2-y^2}$ character is $\beta\langle 165\rangle$, but the electron density resides predominantly on the porphyrin, mainly involving N atom σ-orbitals.

Figure 4a,b shows the experimental and calculated spectra of H_2O−Fe(III)PPIX. The calculated spectrum obtained using TD-DFT with PBE0/LANL2DZ:LANL2DZdp is in excellent agreement with experiment. When the LANL2DZ basis set, which excludes diffuse and polarization functions, was used to calculate the spectrum, agreement was not as satisfactory. Other functionals (CAM-B3LYP, LC-wPBE)[58,59] or an alternative method CI-Singles (CIS)[60] gave poor agreement (see Supporting Information, Figure S5). Both the Soret peak (395 vs 399 nm) and the putative Q-band (510 vs 532 nm) are slightly overestimated in energy in the computed spectrum. The putative charge transfer peak at 581 nm is substantially

Table 2. Charge Contributions of β-Spin MOs of H_2O−Fe(III)PPIX Calculated with PBE0/LANL2DZ:LANL2DZdp Using the OPBE Optimized Geometry[a]

				contribution (%)				
orbital		label[b]	energy (eV)	Fe	H_2O	porphyrin[d]	vinyl	propionic[e]
$\beta\langle 166\rangle$		$b_{2u}(\pi^*)$	−1.209	0	0	94	5	1
$\beta\langle 165\rangle$		$d_{x^2-y^2}$	−1.972	22	0	77	0	0
$\beta\langle 164\rangle$		$e_g(\pi^*)$	−2.499	4	0	92	1	1
$\beta\langle 163\rangle$		$e_g(\pi^*)$	−2.520	5	1	91	2	1
$\beta\langle 162\rangle$		d_{z^2}	−3.031	39	4	55	2	0
$\beta\langle 161\rangle$		d_{xy}	−3.460	75	0	24	0	1
$\beta\langle 160\rangle$		d_π	−3.688	49	2	47	1	1
$\beta\langle 159\rangle$	LUMO	d_π	−3.897	44	0	53	1	2
$\beta\langle 158\rangle$	HOMO	$a_{1u}(\pi)$	−5.784	0	0	96	3	1
$\beta\langle 157\rangle$		$a_{2u}(\pi)$	−5.935	3	0	95	1	1
$\beta\langle 156\rangle$		$b_{2u}(\pi)$	−6.579	1	0	80	18	1
$\beta\langle 155\rangle$		$a_{2u}'(\pi)$	−6.807	3	0	84	11	3
$\beta\langle 154\rangle$		–[c]	−6.994	4	1	87	4	4
$\beta\langle 153\rangle$		–[c]	−7.139	4	0	89	1	6
$\beta\langle 152\rangle$		$e_g(\pi)$	−7.993	2	0	87	10	1
$\beta\langle 151\rangle$		$e_g(\pi)$	−8.031	1	0	90	7	2
$\beta\langle 150\rangle$		–[c]	−8.463	0	0	80	4	15
$\beta\langle 149\rangle$		–[c]	−8.481	0	0	52	0	48
$\beta\langle 148\rangle$		–[c]	−8.504	1	0	80	15	4

[a] All orbitals in the lower half of the table are occupied. [b] In the case of π-orbitals, symmetry labels refer to related orbitals in porphinate, which has idealized D_{4h} symmetry. See Supporting Information (Figure S4) for corresponding porphinate MOs. [c] No corresponding porphinate orbital can be identified. [d] Includes methyl substituents. [e] Includes methylene and carboxylic acid groups.

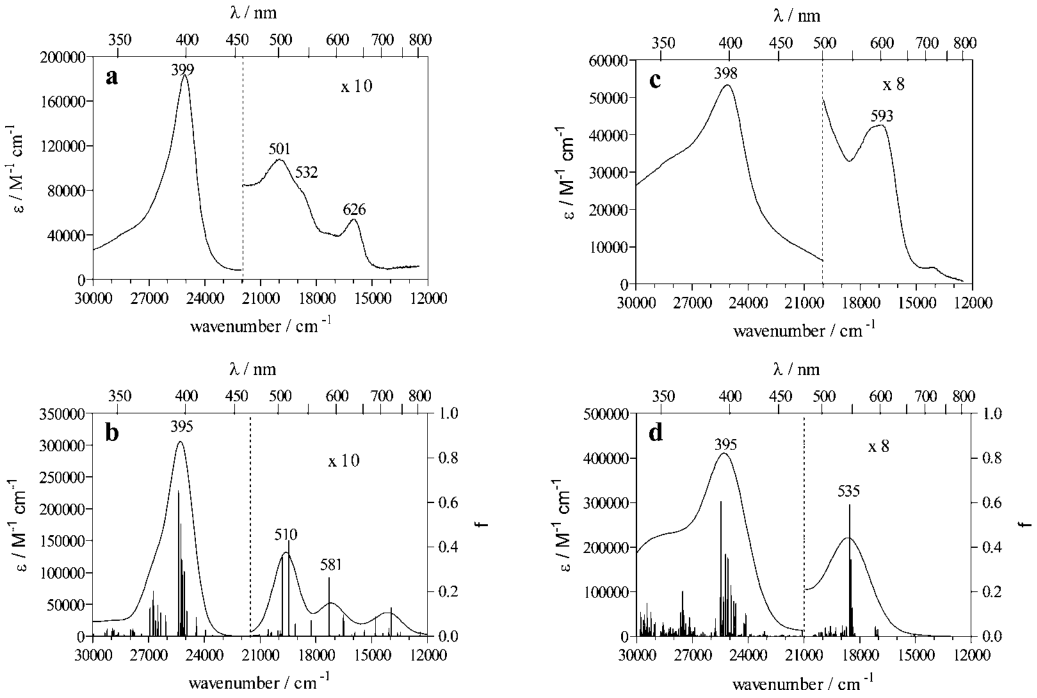

Figure 4. Experimental (a and c) and computed (b and d) UV−visible spectra of H_2O−Fe(III)PPIX (a and b) and μ-$[\text{Fe(III)PPIX}]_2O$ (c and d). Experimental spectra were recorded in (a) acidified aqueous acetone (5.64 M), pH 2 and (b) alkaline aqueous DMSO (5.64 M), pH 12. In spectra b and d, vertical bars are the underlying calculated excitations, with oscillator strengths given on the right axis.

overestimated in energy relative to the experimental peak at 626 nm.

In the calculated spectrum a limited number of one-electron transitions account for the major features between 12 500 cm^{-1} (800 nm) and 28 000 cm^{-1} (357 nm). A simplified description of the β-spin transitions contributing 5% or more to the calculated excitations is illustrated in Scheme 1. The numbering system that we have chosen to employ in this description combines pairs of one-electron transitions terminating in unoccupied MOs that are degenerate in strict D_{4h} symmetry. These correspond to the unoccupied d_π-orbitals ($\beta\langle 159\rangle$ and $\beta\langle 160\rangle$) and the π^*-orbitals that correspond to $e_g(\pi^*)$ in

Scheme 1

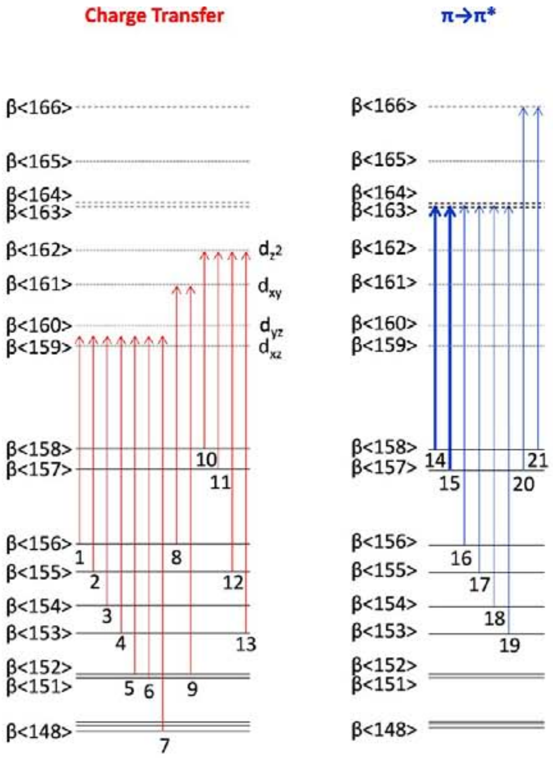

Energy cm^{-1} (nm)	f	Dominant Transitions
13933 (717.7)	0.0127	10(24%) + 1(21%) + **15(26%)** + **14(13%)** + (···)
14789 (676.2)	0.0087	3(49%) + 2(21%) + 1(14%) + (···)
16510 (605.7)	0.0096	**14(34%)** + **15(18%)** + 3(16%) + 1(10%) + 4(10%) + (···)
17283 (578.6)	0.0264	4(27%) + **15(24%)** + **14(21%)** + 2(13%) + (···)
18235 (548.4)	0.0070	4(39%) + 2(20%) + **14(16%)** + **15(12%)** + (···)
19102 (523.5)	0.0055	**14(22%)** + 3(18%) + 4(12%) + 11(11%) + 2(10%) + **15(10%)** + (···)
19444 (514.3)	0.0429	**14(46%)** + **15(35%)** + (···)
19798 (505.1)	0.0354	4(23%) + **15(28%)** + **14(22%)** + (···)
23912 (418.2)	0.0268	13(40%) + 18(13%) + 12(12%) + 5(10%) + (···)
24414 (409.6)	0.0846	5(40%) + (···)
24925 (401.2)	0.1130	6(64%) + (···)
25063 (399.0)	0.2906	17(20%) + 16(20%) + **15(14%)** + (···)
25170 (397.3)	0.3395	5(17%) + **15(16%)** + 17(15%) + **14(10%)** + (···)
25246 (396.1)	0.5026	16(29%) + 17(22%) + **15(14%)** + **14(11%)** + (···)
25381 (394.0)	0.6522	16(25%) + **15(21%)** + **14(16%)** + 17(10%) + (···)
26062 (383.7)	0.0920	5(48%) + 17(10%) + (···)
26337 (379.7)	0.1052	6(50%) + 21(11%) + (···)
26483 (377.6)	0.1391	16(45%) + 18(20%) + (···)
26624 (375.6)	0.0696	16(57%) + 18(10%) + (···)
26731 (374.1)	0.2018	19(45%) + 16(14%) + 18(12%) + (···)
26918 (371.5)	0.1279	19(48%) + 18(11%) + (···)
27360 (365.5)	0.0086	20(30%) + (···)
27755 (360.3)	0.0191	17(53%) + 20(12%) + (···)
27785 (359.9)	0.0079	9(66%) + (···)
27832 (359.3)	0.0314	21(27%) + 9(18%) + (···)
27972 (357.5)	0.0292	17(46%) + 18(15%) + (···)

porphine ($\beta\langle 163\rangle$ and $\beta\langle 164\rangle$). For example, the $\pi\rightarrow d_\pi$ charge transfer transitions $\beta\langle 156\rangle\rightarrow\beta\langle 159\rangle$ and $\beta\langle 156\rangle\rightarrow\beta\langle 160\rangle$ are both labeled CT(1). In addition, all of the β-spin $\pi\rightarrow\pi^*$ transitions shown in Scheme 1 have α-spin counterparts that contribute significantly to the computed spectrum. Such pairs of transitions are represented by a single transition number in the tabulated data in Scheme 1. The transitions labeled CT(8)−CT(13) all represent genuine one electron transitions. Only combined or single transitions contributing 10% or more to a given excitation are listed in the tabulated data, together with the oscillator strength (f) or each excitation.

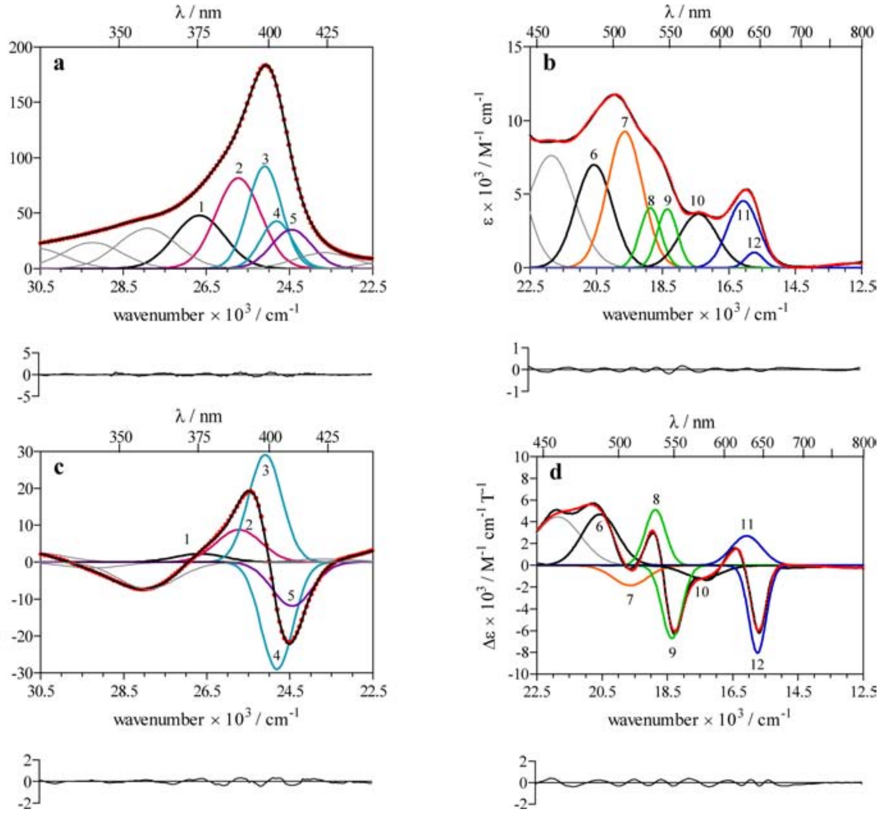

Figure 5. Absorbance (a and b) and MCD (c and d) spectra of H_2O−Fe(III)PPIX recorded at room temperature. In each case absorbance and MCD spectra were simultaneously fitted to eighteen Gaussian functions. Bands discussed in the text are numbered on the spectra. Residuals are shown below each spectrum. Red dots represent the observed spectrum and solid black lines the sum of the fitted functions. Solvent conditions are as in Figure 4a.

In the energy range of interest (12 500−28 000 cm^{-1}), there are 46 excitations in the computed spectrum. No excitation corresponds to any single one-electron transition. Rather, all of the excitations consist of multiple one-electron transitions with varying degrees of configurational mixing. Nine strong excitations account for the major features of the computed spectroscopic envelope between 25 500 and 15 000 cm^{-1} (392 and 667 nm). Four closely spaced excitations at 25 381, 25 246, 25 170, and 25 063 cm^{-1} (394, 396, 397, and 399 nm) give rise to the Soret envelope with a peak maximum at 25 316 cm^{-1} (395 nm). All four are dominated by $\pi \to \pi^*$ transitions, with substantial contributions from transitions $\pi \to \pi^*(14)$ and $\pi \to \pi^*(15)$ (shown in bold in Scheme 1), which correspond to $a_{1u}(\pi)/a_{2u}(\pi) \to e_g(\pi^*)$ in porphine and have previously been suggested to account for the B-band of porphyrins in accordance with Gouterman's four-orbital model.[23,61] However, it is noteworthy that two other transitions, $\pi \to \pi^*(16)$ and $\pi \to \pi^*(17)$, make a larger overall contribution to these four excitations. In addition, there is a small, but significant contribution from CT(5) to the excitation at 25 170 cm^{-1} (397 nm). Two prominent excitations occurring at 19 798 and 19 444 cm^{-1} (505 and 514 nm) give rise to the envelope with a peak maximum at 19 608 cm^{-1} (510 nm). The excitation at 19 444 cm^{-1} is overwhelmingly dominated by the transitions $\pi \to \pi^*(14)$ and $\pi \to \pi^*(15)$. The second excitation also consists of a major contribution from these two $\pi \to \pi^*$ transitions, albeit with a minor, but significant, involvement of the charge transfer transition CT(4) (see Scheme 1). In accordance with the Gouterman model, the prominence of the $\pi \to \pi^*(14)$ and $\pi \to \pi^*(15)$ transitions in this region of the spectrum identifies this as the Q-band. Finally, the band envelope with a peak maximum at 17 212 cm^{-1} (581 nm) is made up of three relatively strong excitations at 18 235, 17 283, and 16 510 cm^{-1} (548, 579, and 606 nm). These three excitations consist of strongly admixed $\pi \to \pi^*$ and $\pi \to d_\pi$ charge transfer transitions involving $\pi \to \pi^*(14)$, $\pi \to \pi^*(15)$, CT(1), CT(2), CT(3), and CT(4) (see Scheme 1 for details).

The experimental UV−visible absorbance and MCD spectra of H_2O−Fe(III)PPIX are presented in Figure 5. These spectra can be used as a fingerprint for identification of this species. In particular, the MCD spectrum, which has not previously been reported, is markedly different from that of other metal complexes of PPIX, including the recently disclosed HO-Fe(III)PPIX,[29] as well as μ-[Fe(III)PPIX$]_2$O, which we describe below. The most notable distinguishing feature is the absence of an intense derivative-shaped peak in the low-energy portion of the spectrum. By contrast, in HO-Fe(III)PPIX, Ga(III)PPIX, and Zn(II)PPIX,[29] as well as μ-[Fe(III)PPIX$]_2$O, this feature is as intense, or almost as intense, as the Soret peak. On the other hand, in cytochrome P450$_{cam}$, which also contains high-spin $S = {}^5/_2$ Fe(III)PPIX, but with an axial cysteine ligand, a similar spectrum to ours is observed.[28]

The spectroscopic envelope of H_2O−Fe(III)PPIX consists of numerous overlapping bands. On account of the very broad features of the UV−visible absorbance spectrum, a unique fit to a set of Gaussian functions is impossible to attain without additional information. On the other hand, the structure present in the MCD spectrum allows far better separation of individual bands. Under the rigid shift approximation, the band shape is not significantly affected by the presence of a magnetic

Table 3. Component Band Positions Obtained from Deconvolution of UV−Visible Absorbance and MCD Spectra of H_2O−Fe(III)PPIX and μ-[Fe(III)PPIX]$_2$O[a,b,c]

experimental		computed	
		H_2O−Fe(III)PPIX	
energy range 26 500−24 000 cm^{-1} (Soret)			energy range 26 500−24 000 cm^{-1} (Soret)
band 2	25 728 (389)	25 381 (394)	$\pi\to\pi^*(16)$, **$\pi\to\pi^*(15)$**, **$\pi\to\pi^*(14)$**, $\pi\to\pi^*(17)$
band 3	25 095 (398)	25 246 (396)	$\pi\to\pi^*(16)$, $\pi\to\pi^*(17)$, **$\pi\to\pi^*(15)$**, **$\pi\to\pi^*(14)$**
band 4	24 810 (403)	25 170 (397)	CT(5), **$\pi\to\pi^*(15)$**, $\pi\to\pi^*(17)$, **$\pi\to\pi^*(14)$**
band 5	24 447 (409)	25 063 (399)	$\pi\to\pi^*(17)$, $\pi\to\pi^*(16)$, **$\pi\to\pi^*(15)$**
energy range 20 000−18 000 cm^{-1} (Q/Q$_V$)			energy range 21 000−19 000 cm^{-1} (Q)
band 7	19 636 (509)[c]	19 798 (501) 19 444 (514)	CT(4), **$\pi\to\pi^*(15)$**, **$\pi\to\pi^*(14)\pi\to\pi^*(14)$**, **$\pi\to\pi^*(15)$**
band 8	18 865 (530)		
band 9	18 356 (545)		
energy range 18 000−15 000 cm^{-1}			energy range 18 000−16 000 cm^{-1}
band 10	17 418 (574)	18 235 (548)	CT(4), CT(2), **$\pi\to\pi^*(14)$**, **$\pi\to\pi^*(15)$**
band 11	16 070 (622)	17 283 (579)	CT(4), **$\pi\to\pi^*(15)$**, **$\pi\to\pi^*(14)$**, CT(2)
band 12	15 736 (635)	16 510 (606)	**$\pi\to\pi^*(14)$**, **$\pi\to\pi^*(15)$**, CT(3), CT(1), CT(4)
		μ-[Fe(III)PPIX]$_2$O	
energy range 26 500−24 000 cm^{-1} (Soret)			energy range 26 500−24 800 cm^{-1} (Soret)
		25 739 (389)	$\pi\to\pi^*(21)$, $\pi\to\pi^*(23)$, $\pi\to\pi^*(19)$
		25 475 (393)	$\pi\to\pi^*(17)$, **$\pi\to\pi^*(16)$**, **$\pi\to\pi^*(15)$**, CT(7)
band 1	25 913 (386)	25 448 (393)	$\pi\to\pi^*(17)$, $\pi\to\pi^*(23)$, $\pi\to\pi^*(20)$
band 2	25 017 (400)	25 352 (394)	$\pi\to\pi^*(17)$, $\pi\to\pi^*(20)$, $\pi\to\pi^*(23)$
band 3	24 363 (410)	25 331 (395)	$\pi\to\pi^*(17)$, CT(7), CT(8), $\pi\to\pi^*(23)$, **$\pi\to\pi^*(16)$**
		25 197 (397)	$\pi\to\pi^*(17)$, $\pi\to\pi^*(23)$, $\pi\to\pi^*(20)$
		25 088 (399)	$\pi\to\pi^*(17)$, $\pi\to\pi^*(18)$, $\pi\to\pi^*(22)$, CT(7)
		24 911 (401)	CT(12), $\pi\to\pi^*(22)$, $\pi\to\pi^*(19)$
energy range 15 500−19 000 cm^{-1}			energy range 15 500−19 000 cm^{-1}
band 4	17 984 (556)[e]		
band 5	17 373 (576)[e]	18 536 (540)	CT(7), **$\pi\to\pi^*(15)$**, CT(6), **$\pi\to\pi^*(16)$**
band 6	16 729 (598)	18 458 (542)	**$\pi\to\pi^*(15)$**, CT(7), CT(1), CT(6)
band 7	16 065 (622)		

[a] Prominent calculated excitations obtained from TD-DFT calculations (PBE0/LANL2DZ:LANL2DZdp) making up the major spectroscopic envelope features are shown for comparison. [b] Transitions shown in bold have counterparts in porphinate that correspond to those involved in Gouterman's four-orbital model. [c] Band positions and excitations in wavenumbers (cm^{-1}) with wavelength in parentheses (nm). [d] Probable Q$_V$-band. [e] Possible vibronic bands.

field.[62,63] The value of simultaneously fitting both the absorbance and MCD spectra is that uncertainty in the deconvolution of the spectrum is reduced. This approach has been successfully used in the investigation of metalloporphyrins and related compounds.[23,24,64] Using this method, we have deconvoluted both the absorbance and MCD spectra of H_2O−Fe(III)PPIX with eighteen Gaussian functions (Figure 5 and Supporting Information, Table S2). Care was taken to fit the spectra with the smallest number of bands that gave a satisfactory fit to the spectroscopic envelope. In particular, in the parts of the spectra corresponding to the numbered bands in Figure 5, great caution was exercised to ensure that each fitted band corresponded to a noticeable feature (peak or obvious shoulder) in either the UV−visible or MCD spectrum or both. The fitting to relatively featureless regions of the spectra (corresponding to un-numbered bands) is less certain.

MCD spectra of paramagnetic molecules exhibit three types of spectroscopic terms, A-terms, giving rise to derivative-shaped bands, and B- and C-terms, giving rise to Gaussian bands. The temperature-dependent C-terms, which are dominant in paramagnetic species, are most prominent at low temperature but can only be definitively assigned using variable-temperature MCD, which allows the cancellation of A- and B-terms. Unequivocal assignment of the individual bands in H_2O−Fe(III)PPIX would require this technique. Nevertheless, even in the absence of this instrumentation, some insight can be obtained into the observed spectra with the aid of the computed UV−visible absorbance data. The minimum number of fitted bands in the most important (numbered) regions of the spectrum does appear to correspond to an equivalent number of strong excitations in the computed spectrum. Thus, four fitted bands in the Soret region (bands 2−5) likely correspond to the four intense B-band excitations seen in the related part of the computed spectrum (see Table 3). Similarly, the two fitted bands 8 and 9 seem to correspond to computed Q-band excitations at 19 798 and 19 444 cm^{-1} (505 and 514 nm), while bands 10, 11, and 12 may match the three prominent excitations calculated at 18 235, 17 283, and 16 510 cm^{-1} (548, 579, and 606 nm).

If this putative assignment is correct, bands 2−5 involve transitions $\pi\to\pi^*(14)$, $\pi\to\pi^*(15)$, $\pi\to\pi^*(16)$, and $\pi\to\pi^*(17)$ with a very small CT(5) charge transfer component and bands 8 and 9 comprise transitions $\pi\to\pi^*(14)$ and $\pi\to\pi^*(15)$ with a small CT(4) contribution. The observation of oppositely signed Gaussian functions (bands 3 and 4, 2 and 5, and 8 and 9) forming apparent pseudo-A-term features seems to support this proposal and are in agreement with the long-established interpretation of the similar spectrum of aquometmyoglobin (H_2O-metMb).[21] Band 7, which does not appear to correspond to a computed feature, may be the Q$_V$-band, as it

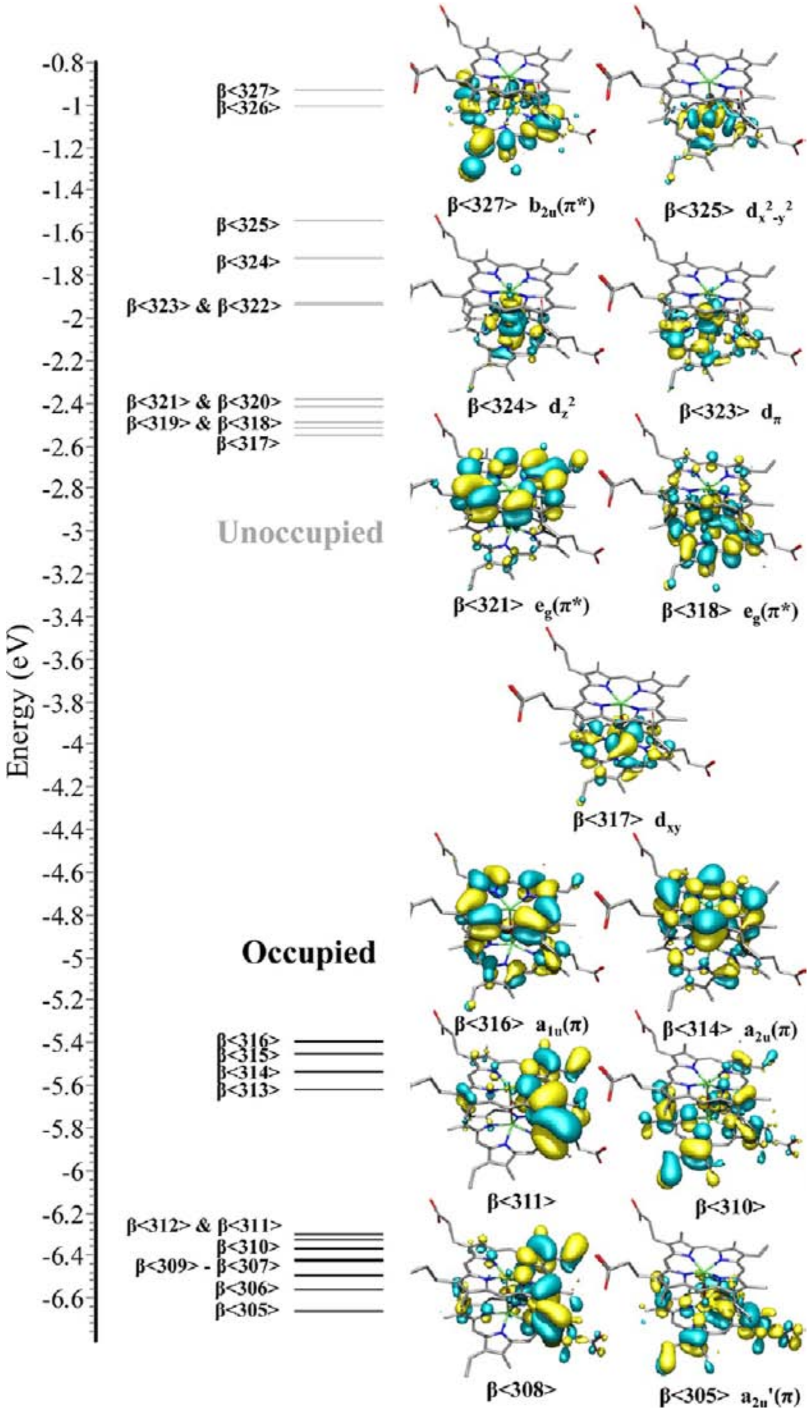

Figure 6. β-Spin MO diagram of μ-[Fe(III)PPIX]$_2$O showing selected MOs.

occurs 1280 cm^{-1} higher in energy than band 9. The positive MCD component may underlie band 6 and is not resolved. Bands 10−12, which have previously been assigned as $\pi \rightarrow d_\pi$ charge transfer bands in H_2O-metMb,[21] or more recently as the $a_{1u}/a_{2u}(\pi) \rightarrow e_g(\pi^*)$ Q-band in the case of HO-Fe(III)PPIX,[29] in fact appears to consist of a combination of these transitions. Finally, the region of the spectrum between the B- and Q_V-bands is poorly resolved, but based on computational evidence, a series of largely charge-transfer excitations would be expected here (see Scheme 1). A summary of the major features of the experimental and computed spectra is presented in Table 3.

μ-[Fe(III)PPIX]$_2$O (spin paired, S = 0). The MOs associated with the major calculated β-spin transitions in μ-[Fe(III)-PPIX]$_2$O, together with the corresponding MO diagram, are presented in Figure 6. Since broken symmetry was used to treat μ-[Fe(III)PPIX]$_2$O as fully antiferromagnetically coupled, unlike H_2O−Fe(III)PPIX, every β-spin MO with substantial metal d-orbital character on the one Fe(III) ion has an almost identical α-spin counterpart on the other. Once again, for the sake of brevity, only β-spin MOs are discussed. Orbital contributions from porphyrin, vinyl, and propionate side chains and Fe(III) ions of each Fe(III)PPIX moiety as well as the O^{2-} bridging ligand are shown in Table 4. Seven of the π and π*

Table 4. Charge Contributions of β-Spin MOs of μ-[Fe(III)PPIX]$_2$O Calculated with PBE0/LANL2DZ:LANL2DZdp Using the OPBE Optimized Geometry[a,b]

			composition (%)								
			Fe		porphyrin[f]		vinyl		propionate[g]		O^{2-}
orbital	label[c]	energy (eV)	1	2	1	2	1	2	1	2	
$\beta\langle 327\rangle$	$b_{2u}(\pi^*)$	−0.943	9	1	65	14	9	0	2	0	0
$\beta\langle 326\rangle$	$b_{2u}(\pi^*)$	−1.014	0	4	16	69	0	8	0	2	0
$\beta\langle 325\rangle$	$d_{x^2-y^2}$	−1.559	16	0	75	7	1	0	1	0	0
$\beta\langle 324\rangle$	d_{z^2}	−1.735	31	8	36	16	0	0	1	0	7
$\beta\langle 323\rangle$	d_π	−1.938	20	2	51	24	1	0	0	0	2
$\beta\langle 322\rangle$	d_π	−1.951	27	1	58	9	1	0	1	0	2
$\beta\langle 321\rangle$	$e_g(\pi^*)$	−2.392	3	17[e]	34	45	0	1	0	0	0
$\beta\langle 320\rangle$	$e_g(\pi^*)$	−2.427	5	12[e]	21	59	0	1	0	1	0
$\beta\langle 319\rangle$	$e_g(\pi^*)$	−2.505	17[e]	8	35	38	1	1	0	0	1
$\beta\langle 318\rangle$	$e_g(\pi^*)$	−2.529	24[e]	3	48	21	1	0	1	0	1
$\beta\langle 317\rangle$ LUMO	d_{xy}	−2.561	35	1	34	27	1	0	1	1	0
$\beta\langle 316\rangle$ HOMO	$a_{1u}(\pi)$	−5.409	0	0	43	54	1	1	0	1	0
$\beta\langle 315\rangle$	$a_{1u}(\pi)$	−5.463	0	0	45	51	1	1	1	1	0
$\beta\langle 314\rangle$	$a_{2u}(\pi)$	−5.549	2	5	32	58	0	0	1	1	0
$\beta\langle 313\rangle$	$a_{2u}(\pi)$	−5.637	5	2	65	26	1	0	1	0	0
$\beta\langle 312\rangle$	–[d]	−6.312	1	1	67	13	16	0	1	0	1
$\beta\langle 311\rangle$	–[d]	−6.339	0	2	14	68	0	14	0	1	0
$\beta\langle 310\rangle$	–[d]	−6.381	1	0	60	24	8	2	3	0	2
$\beta\langle 309\rangle$	–[d]	−6.431	3	1	55	27	1	3	8	0	1
$\beta\langle 308\rangle$	–[d]	−6.435	4	5	30	46	1	9	3	1	1
$\beta\langle 307\rangle$	–[d]	−6.506	1	4	6	74	0	1	0	14	0
$\beta\langle 306\rangle$	–[d]	−6.570	3	5	18	59	0	1	1	14	1
$\beta\langle 305\rangle$	$a_{2u}'(\pi)$	−6.674	3	4	55	20	4	0	12	1	0

[a] The labels 1 and 2 refer to the first and second Fe(III)porphyrin in the dimer, respectively. [b] All orbitals in the bottom half of the table are filled. [c] in the case of π-orbitals, symmetry labels refer to related orbitals in monomeric porphinate which has idealized D_{4h} symmetry. [d] No corresponding porphinate orbital can be identified. [e] Fe p_x and p_y. [f] Includes methyl substituents. [g] includes methylene and carboxylate groups.

MOs exhibit substantial contributions (>30%) from atoms on both porphyrins ($\beta\langle 308\rangle$, $\beta\langle 309\rangle$, $\beta\langle 314\rangle$ to $\beta\langle 316\rangle$, $\beta\langle 319\rangle$ and $\beta\langle 321\rangle$). The remaining 11 have contributions mainly situated on a single porphyrin. An interesting observation is that the π^* MOs $\beta\langle 318\rangle$ to $\beta\langle 321\rangle$ have notable contributions from Fe(III) 3p_x- and 3p_y-orbitals. Similar behavior is not observed in H_2O−Fe(III)PPIX and arises from doming of the porphyrin moieties in μ-[Fe(III)PPIX]$_2$O. The resulting displacement of the Fe(III) centers out of the plane of the porphyrin N-atoms (0.56 Å) allows net overlap of these p-orbitals with the porphyrin π-orbitals. This is not the case in H_2O−Fe(III)PPIX, which exhibits much less doming (0.27 Å out of the N-atom plane) with the consequence that these orbitals lie largely in the nodal plane of the π-system.

The unfilled MOs with Fe(III) d-orbital character in μ-[Fe(III)PPIX]$_2$O have substantially smaller contributions from these metal atomic orbitals than the corresponding MOs in H_2O−Fe(III)PPIX (compare Tables 2 and 4). Unlike H_2O−Fe(III)PPIX, there is a noticeable axial ligand contribution to the MO with Fe(III) d_{z^2}-orbital character ($\beta\langle 324\rangle$). A striking feature of μ-[Fe(III)PPIX]$_2$O is that while the ordering of the filled MOs in the energy range of interest is similar to that of H_2O−Fe(III)PPIX, there is a reordering of the unfilled MOs, such that the two d_π-orbitals ($\beta\langle 322\rangle$ and $\beta\langle 323\rangle$) and the d_{z^2}-orbital ($\beta\langle 324\rangle$) lie above the lowest energy π^*-orbitals ($\beta\langle 318\rangle$ to $\beta\langle 321\rangle$). This results from a considerable increase in the energy of the MOs with metal d-orbital character. On the other hand, there is little change in the energy of the π^*-orbitals.

The calculated spectrum of antiferromagnetically coupled μ-[Fe(III)PPIX]$_2$O computed as described for H_2O−Fe(III)PPIX is presented in Figure 4. The features of the experimental spectrum of this species (Figure 4c), which differ markedly from that of H_2O−Fe(III)PPIX, are at first sight reproduced well in the computed spectrum (Figure 4d). The main Soret peak computed at 395 nm is slightly overestimated in energy relative to the experimental peak at 398 nm, while the low-energy envelope peak is substantially overestimated (535 vs 593 nm). Owing to the fact that μ-[Fe(III)PPIX]$_2$O has almost twice as many MOs as H_2O−Fe(III)PPIX, there are many more one-electron transitions that contribute to the calculated spectrum between the limits of 12 500 and 28 000 cm^{-1}. For the sake of facilitating discussion, we have grouped transitions along the lines described for H_2O−Fe(III)PPIX above. More specifically, we have grouped transitions between MOs that are degenerate in the idealized μ-[Fe(III)P]$_2$O molecule (see Supporting Information, Figure S6 and Table S3). Thus, all transitions to α-spin MOs are labeled with the same number as the corresponding transitions to β-spin MOs. In addition, we have grouped together transitions to the eight MOs $\alpha/\beta\langle 318\rangle$ to $\alpha/\beta\langle 321\rangle$. These derive from the degenerate pair of $e_g(\pi^*)$ MOs of porphine, but are not strictly degenerate even in μ-[Fe(III)P]$_2$O because of doming of the porphyrin, with consequent in-phase and out-of-phase contributions from Fe(III) 3p_x- and 3p_y-orbitals. Nevertheless, these eight MOs lie close in energy and can be thought of as a single group. Finally, we have grouped together transitions to the d_π-orbitals ($\alpha/\beta\langle 322\rangle$ and $\alpha/\beta\langle 323\rangle$). These transitions are illustrated in

Scheme 2

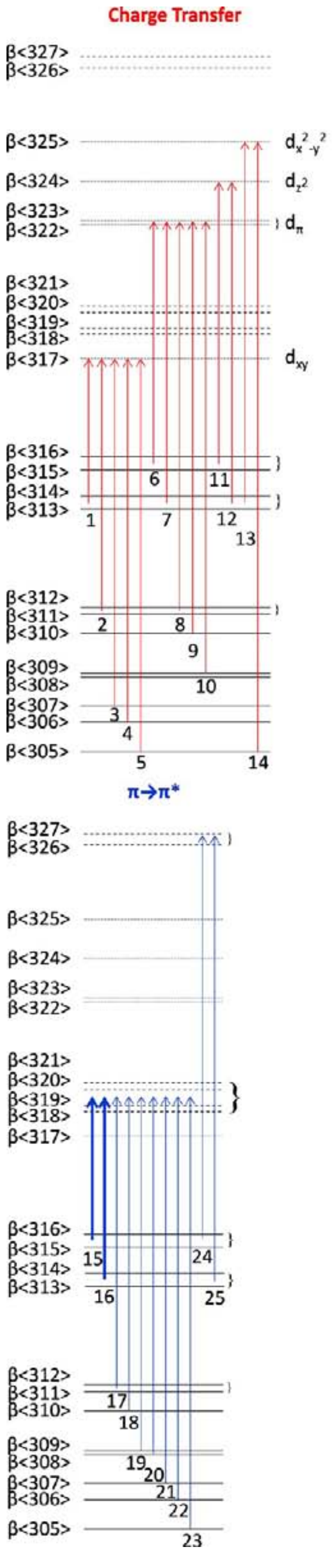

Energy cm^{-1} (nm)	f	Dominant Transitions
17129 (583.8)	0.0058	**16(37%)** + **15(31%)** +7(13%) + 1(6%) + (···)
18362 (544.6)	0.0052	1(62%) + **16(9%)** + **15(7%)** + 7(5%) + (···)
18391 (543.8)	0.0160	1(59%) + **16(9%)** + 7(8%) + (···)
18458 (541.8)	0.0430	**15(28%)** + 7(20%) + 1(17%) + 6(6%) + (···)
18536 (539.5)	0.0739	7(33%) + **15(30%)** + 6(9%) + **16(6%)** + (···)
18707 (534.6)	0.0055	**15(80%)** + (···)
18923 (528.5)	0.0059	**15(38%)** + 17(18%) + 7(5%) + (···)
19545 (511.7)	0.0056	**16(38%)** + 6(6%) + (···)
21085 (474.3)	0.0263	12(70%) + **16(5%)** + (···)
22092 (452.7)	0.0053	13(80%) + 14(6%) + (···)
22175 (451.0)	0.0065	13(78%) + 14(6%) + (···)
23122 (432.5)	0.0225	7(22%) + 18(19%) +19(6%) + (···)
23192 (431.2)	0.0097	7(50%) + (···)
23380 (427.7)	0.0053	7(21%) + 18(18%) + 19(11%) + 17(9%) + (···)
23824 (419.7)	0.0097	7(23%) + **16(14%)** + 18(5%) + (···)
23916 (418.1)	0.0072	7(17%) + **16(20%)** + **15(14%)** + (···)
24119 (414.6)	0.1009	17(33%) + 18(11%) + (···)
24228 (412.7)	0.0582	17(24%) + 18(8%) + 22(8%) + 2(7%) + (···)
24350 (410.7)	0.0085	17(26%) + 22(7%) + (···)
24456 (408.9)	0.0058	17(18%) + 11(8%) + 22(7%) + 18(7%) + (···)
24661 (405.5)	0.1467	12(29%) + 19(7%) + 22(7%) + (···)
24759 (403.9)	0.1577	12(33%) + 17(13%) + (···)
24819 (402.9)	0.0111	12(34%) + 22(6%) +19(6%) + (···)
24853 (402.4)	0.0090	12(48%) + 19(7%) + (···)
24911 (401.4)	0.2280	12(20%) + 22(9%) + 19(6%) + (···)
24959 (400.7)	0.0146	19(15%) + 22(8%) + 23(8%) + 5(8%) + (···)
25006 (399.9)	0.0105	5(55%) + 23(11%) + (···)
25021 (399.7)	0.0159	5(47%) + 23(8%) + (···)
25088 (398.6)	0.3523	17(7%) + 18(6%) + 22(6%) + 7(5%) + (···)
25197 (396.9)	0.3690	17(22%) + 7(7%) + 8(6%) + 23(5%) + **16(5%)** + (···)
25331 (394.8)	0.1767	17(17%) + 20(15%) + 23(5%) + (···)
25352 (394.4)	0.0702	17(29%) + 23(6%) + 20(5%) + (···)
25448 (393.0)	0.6045	17(20%) + **16(7%)** + **15(5%)** + 7(5%) + (···)
25475 (392.5)	0.1896	17(34%) + 23(12%) + (···)
25739 (388.5)	0.0793	21(25%) + 23(9%) + 19(7%) + (···)
25816 (387.4)	0.0181	21(34%) + 23(6%) + 20(6%) + 10(6%) + (···)
25965 (385.1)	0.0153	21(31%) + 10(6%) + 23(6%) + 20(5%) + (···)
26303 (380.2)	0.0080	17(38%) + 24(17%) + (···)
26333 (379.8)	0.0099	24(29%) + 17(28%) + (···)
26429 (378.4)	0.0184	20(21%) + 17(13%) + 21(5%) + (···)
26516 (377.1)	0.0088	24(26%) + 17(11%) + 25(8%) + 21(8%) + (···)
26872 (372.1)	0.0399	17(22%) + 20(12%) + (···)
26948 (371.1)	0.0218	17(49%) + 20(16%) + (···)
26987 (370.6)	0.0191	17(35%) + 20(11%) + 4(8%) + (···)
27000 (370.4)	0.0056	3(52%) + 21(7%) + (···)
27038 (369.9)	0.0056	3(61%) + 21(9%) + (···)
27070 (369.4)	0.0209	3(20%) + 20(16%) + 19(6%) + (···)
27100 (369.0)	0.0384	23(17%) + 3(14%) + 8(8%) + 17(6%) + 22(5%) + (···)
27160 (368.2)	0.0848	20(22%) + 22(11%) + 23(10%) + (···)
27183 (367.9)	0.0172	23(52%) + 4(10%) + 17(6%) + (···)
27232 (367.2)	0.0076	22(21%) + 23(14%) + 4(10%) + 17(7%) + (···)
27345 (365.7)	0.0561	17(16%) + 18(15%) +20(7%) + 8(7%) + 4(7%) + (···)
27367 (365.4)	0.0279	17(27%) + 20(10%) + 8(9%) + 18(7%) + (···)
27409 (364.8)	0.0259	17(26%) + 9(12%) + 23(8%) + 22(7%) + (···)
27473 (364.0)	0.1173	18(22%) + 23(12%) + 20(10%) + 22(7%) + (···)
27507 (363.5)	0.2031	18(19%) + 8(14%) + 20(14%) + (···)
27608 (362.2)	0.1070	8(14%) + 22(14%) + 18(11%) + 23(8%) + 17(6%) + (···)
27725 (360.7)	0.0359	18(24%) + 8(20%) + 21(13%) + 9(6%) + (···)
27748 (360.4)	0.0127	21(26%) + 18(15%) + 20(14%) + 9(9%) + 8(6%) + (···)
27797 (359.8)	0.0055	18(27%) + 8(17%) + 17(6%) + 20(6%) + (···)
27837 (359.2)	0.0110	18(45%) + 21(13%) + 8(10%) + 20(10%) + (···)
27871 (358.8)	0.0224	21(42%) + 8(18%) + 18(5%) + (···)
27931 (358.0)	0.0232	21(41%) + 18(17%) + 10(6%) + (···)
27976 (357.5)	0.0147	21(42%) + 18(12%) + 8(8%) + (···)

Scheme 2 in those cases where they contribute 5% or more to any given excitation.

In the range 12 500−28 000 cm^{-1} there are 147 excitations in the calculated spectrum. As was observed for H_2O−Fe(III)-PPIX, all of these excitations are made up of multiple one-electron transitions with configurational mixing. Similar to the experimental absorbance spectrum, the computed spectroscopic envelope exhibits a number of prominent distinguishing features, namely, a Soret peak at 25 316 cm^{-1} (395 nm) with a very pronounced and broad high energy shoulder, a noticeable broadening on the low energy side of the Soret peak, and a single low-energy peak at 18 692 cm^{-1} (535 nm). Eight excitations with relatively large oscillator strengths make up the computed Soret peak. These excitations consist of mainly π→

π^* transitions, all of which terminate in the orbitals corresponding to $e_g(\pi^*)$ in porphine. They include transitions $\pi\rightarrow\pi^*(15)$ and $\pi\rightarrow\pi^*(16)$, which are the counterparts of the $a_{1u}/a_{2u}(\pi)\rightarrow e_g(\pi^*)$ transitions in D_{4h} porphine (shown in bold in Scheme 2), but the major contributing transitions originate in lower-lying π MOs with no counterparts in porphine. An interesting observation is that these lower-lying MOs have noticeable vinyl character and tend to be localized on the half of the porphyrin ring closest to the vinyl groups. A similar pattern was seen in H_2O−Fe(III)PPIX (corresponding to transitions $\pi\rightarrow\pi^*(16)$ and $\pi\rightarrow\pi^*(17)$ in Scheme 1) and contributes to the complexity of the Soret peak. There is a substantially larger contribution of charge transfer transitions in μ-[Fe(III)-PPIX]$_2$O compared with H_2O−Fe(III)PPIX in this part of the spectrum. The major contributing transitions are CT(7) and CT(8), which are $\pi\rightarrow d_\pi$ transitions and CT(12), which is a $\pi\rightarrow d_{z^2}$ transition. The high energy shoulder of the Soret peak will not be discussed further, owing to the very large number of underlying excitations (see Scheme 2). The broadening on the low-energy side of the Soret peak is the result of a considerable number of excitations, most, but not all, of which involve substantial $\pi\rightarrow d_{z^2}$ charge transfer character (see Scheme 2). Finally, the low-energy peak is dominated by two relatively strong, closely spaced excitations with heavily mixed $\pi\rightarrow\pi^*$ and $\pi\rightarrow d_\pi$ character, which can neither be described as a Q-band nor a charge transfer band. The $\pi\rightarrow\pi^*$ component consists of mainly $\pi\rightarrow\pi^*(15)$ and $\pi\rightarrow\pi^*(16)$, the transitions associated with the Gouterman four-orbital model (see Scheme 2).

The experimental UV−visible absorbance and MCD spectra of μ-[Fe(III)PPIX]$_2$O are presented in Figure 7. Once again we emphasize the utility of employing the MCD spectrum as a fingerprint for the identification of this species. Of particular note in this case is the unusual apparently reversed (negative) A-term feature corresponding to the Soret peak, together with the intense positive A-term feature at low energy. These features make the spectrum quite distinct from those of both H_2O−Fe(III)PPIX (Figure 5) and HO-Fe(III)PPIX as previously reported by Pinter et al.[29] Deconvolution of the spectra, with particular attention to the two main peak envelopes, suggests that the Soret peak is probably not actually a reverse A-term, but rather consists of three Gaussian bands (1, 2, and 3 in Figure 7) with alternating sign similar to that seen in Cl−Fe(III)TPP and in cytochrome P450$_{\mathrm{cam}}$.[24,28] The low-energy peak envelope appears to consist of two strong bands with opposite sign forming a pseudo-A-term in the MCD spectrum (bands 6 and 7). It is possible that two higher-energy bands (bands 4 and 5), which form a weaker pseudo-A-term in the MCD, may represent a vibronic band since they are shifted by about 1280 cm^{-1} relative to bands 6 and 7, close to the difference between the Q- and Q_V-bands in H_2O−Fe(III)PPIX.

Assignment of the experimental spectra of μ-[Fe(III)-PPIX]$_2$O is even more difficult than that of H_2O−Fe(III)PPIX. In addition to the limitations already described in relation to the absence of variable-temperature MCD in the case of H_2O−Fe(III)PPIX and the very much greater number of excitations in the computed spectrum, a further complication is encountered. The spectrum of μ-[Fe(III)PPIX]$_2$O calculated using broken symmetry describes the fully antiferromagnetically coupled diamagnetic molecule. However, as the temperature rises above 0 K, the molecule is thermally excited into weakly paramagnetic states.[65] Thus, the calculated spectrum is not strictly comparable to the experimental spectrum, even at low temperature, let alone at room temperature, thus precluding correlation of fitted bands with calculated excitations.

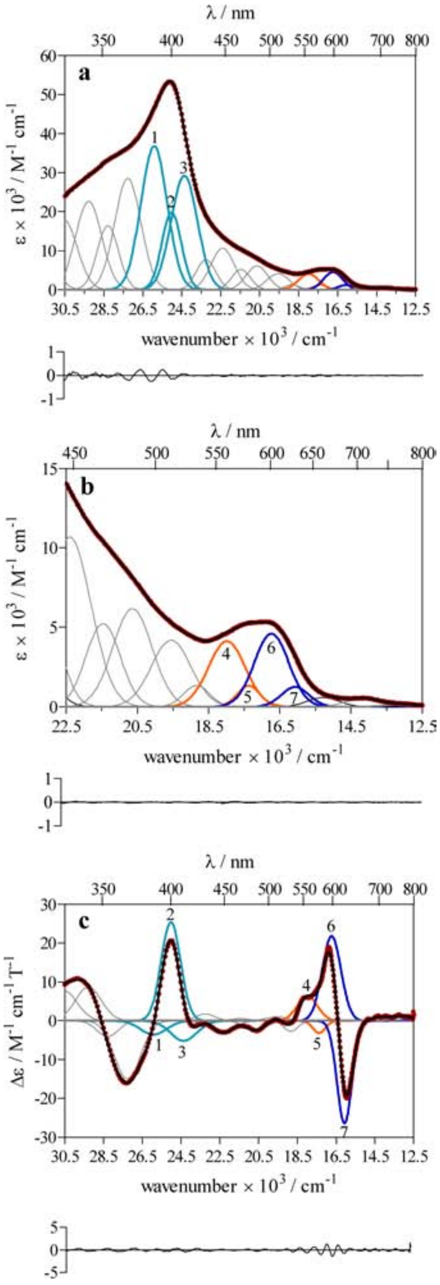

Figure 7. Absorbance (a and b) and MCD (c) spectra of μ-[Fe(III)PPIX]$_2$O recorded at room temperature. In each case, absorbance and MCD spectra were simultaneously fitted to twenty-two Gaussian functions. Residuals are shown below each spectrum. Red dots represent the observed spectrum and black lines the sum of the fitted Gaussian functions. Spectrum b is an enlargement of the lower-energy portion of spectrum a.

As an indication of the effects of antiferromagnetic coupling on the major features of the spectrum, we have compared the computed spectra of the paramagnetic $S = {}^{10}/_2$ and antiferromagnetic $S = 0$ states of μ-[Fe(III)P]$_2$O as a model system (see Supporting Information, Figures S6−S10 and Tables S3 and S4). In the antiferromagnetically coupled model system, the major spectroscopic features are rather similar to those observed in antiferromagnetically coupled μ-[Fe(III)-PPIX]$_2$O. Three major peaks are seen: a Soret peak at 26 954

cm^{-1} (371 nm), consisting of two very closely spaced excitations made up of $a_{1u}/a_{2u}(\pi)\rightarrow e_g(\pi^*)$ transitions, together with a smaller charge transfer component made up mainly of $\pi\rightarrow d_\pi$ transitions; a charge transfer peak at 21 978 cm^{-1} (455 nm) dominated by a single excitation made up almost exclusively of $\pi\rightarrow d_{z^2}$ transitions; and a low-energy peak at 19 802 cm^{-1} (505 nm) dominated by a very closely spaced pair of excitations consisting of almost equal contributions of configurationally mixed $a_{1u}/a_{2u}(\pi)\rightarrow e_g(\pi^*)$ and $\pi\rightarrow d_\pi$ charge transfer transitions. The calculated spectrum of the paramagnetic model system has rather similar prominent features to the antiferromagnetically coupled spectrum. The Soret peak is slightly blue-shifted to 27 100 cm^{-1} (369 nm) and is somewhat less intense, while the low-energy peak is considerably red-shifted to 17 422 cm^{-1} (574 nm). These two peaks are still composed of predominantly $\pi\rightarrow\pi^*$ and $\pi\rightarrow d_\pi$ transitions originating in the four highest occupied MOs, with the former terminating in the four lowest unoccupied π^* MOs. The two most intense excitations underlying the Soret peak have about 10% more charge transfer character than their counterparts in the antiferromagnetically coupled system, while the closely spaced pair of excitations underlying the low-energy peak are predominantly composed of $\pi\rightarrow\pi^*$ transitions, with a substantially smaller $\pi\rightarrow d_\pi$ component than the corresponding excitations in the coupled system. The $\pi\rightarrow d_{z^2}$ excitation is shifted under the low-energy peak envelope, while a new intense $\pi\rightarrow d_\pi$ transition appears between the Soret and low-energy envelopes. Thus, despite changes in the appearance of some MOs and a splitting of the d_π- and d_{z^2}-orbitals as a result of overlap with the axial ligand in the $S = {}^{10}/_2$ case (see Tables S3 and S4 and Figures S6 and S7, Supporting Information), the overall composition of the prominent features of the calculated spectrum remain broadly very similar to those of the antiferromagnetically coupled system, except for the $\pi\rightarrow d_{z^2}$ contribution to the low-energy peak envelope.

In view of the general similarities in the calculated spectra of the paramagnetic and antiferromagnetic forms of μ-[Fe(III)P]$_2$O, it seems reasonable to conclude that at least the overall features of the experimental UV–visible spectrum of μ-[Fe(III)PPIX]$_2$O will not be drastically different from the computed spectrum for the antiferromagnetically coupled state of this species. Specifically, while the Soret peak probably does consist largely of $\pi\rightarrow\pi^*$ transitions, a substantial $\pi\rightarrow d_\pi$ component is likely present, and the low-energy peak probably consists of excitations involving $\pi\rightarrow\pi^*(15)$, $\pi\rightarrow\pi^*(16)$, CT(6), and CT(7) transitions, since the corresponding transitions are observed in all three of the computed μ-oxo dimers. The region between these two peaks may be dominated by charge transfer transitions, either with $\pi\rightarrow d_\pi$ or $\pi\rightarrow d_{z^2}$ character, or both, while the latter transition may make some contribution to the low-energy spectroscopic envelope. More insight into this region of the spectrum could probably be obtained using variable-field MCD, since the calculated transition dipole moments lie more than 70° off the *x,y*-plane in the case of excitations dominated by $\pi\rightarrow d_{z^2}$ transitions calculated for μ-[Fe(III)PPIX]$_2$O. A more definitive assignment would certainly require the use of variable-temperature MCD. Major features of the experimental and calculated spectra are collected in Table 3.

DISCUSSION

DFT-calculated structures obtained using OPBE/LANL2DZ agree well with reported bond lengths in the CSD. The Fe–O bond length of cationic H_2O–Fe(III)PPIX (2.169 Å) is close to the average for all reported crystal structures of Fe(III)-porphyrins with H_2O ligands and lies well within the observed range (1.976–2.951 Å). Of the 15 reported structures in the CSD, only four are five-coordinate. These have an average Fe–O length of 2.06(2) Å and are spread over a narrower range (2.039–2.085 Å). Since this average is about 0.1 Å shorter than the calculated value, we investigated whether the introduction of polarization functions on nonmetal atoms in the form of the LANL2DZdp basis set would reduce this discrepancy. Paulat and Lehnert reported that use of polarization functions for Cl–Fe(III)TPP better described the Fe(III)–Cl bond.[24] In fact, using this basis set we found that the bond lengthened considerably and the axial water ligand adopted an unrealistic orientation in which the O–H bonds lie parallel to the porphyrin. The Fe–N_{por} bond lengths (2.06 Å) are also slightly longer than the average, although they fall within the range observed in the reported crystal structures (1.945–2.061 Å).[56] It must however be emphasized that none of the 15 crystal structures actually involve protoporphyrin IX, and hence, structural differences may not be unexpected. In the case of μ-[Fe(III)PPIX]$_2$O, the computed Fe–O bond length of 1.80 Å is again a little longer than the average for reported Fe(III)–porphyrin μ-oxo dimers, falling just above the observed range (1.740–1.786 Å).[56] Likewise, the Fe–N_{por} bond length (2.13 Å) is somewhat longer than the average and lies marginally above the range observed in crystal structures (2.065–2.102 Å). The Fe–O–Fe angle (178°) lies well within the observed range of 150–180° and is close to the average.[56]

An interesting observation in the case of H_2O–Fe(III)PPIX is that the overall charge on the complex has a significant influence on the length of the axial bond, which lengthens by more than 0.1 Å in going from the cationic to the anionic species. On the other hand, in comparing with the Fe(III)-porphine analogs it is evident that the presence of uncharged methyl, vinyl, and propionic acid substituents on the periphery of the porphyrin has a much smaller effect on axial bond lengths.

IR spectra calculated from the computed structures agree well with experimental results. This demonstrates that the model not only reproduces structural features of these molecules but also their spectroscopic properties. To our knowledge, this is the first time that vibrational spectra have been directly calculated for these specific species (as opposed to smaller, symmetric analogs and β-hematin). Pleasingly, for the most part the calculations confirm previous literature assignment of the spectra.

In this study, the UV–visible spectrum of H_2O–Fe(III)PPIX was initially predicted using TD-DFT with the hybrid PBE0 functional and LANL2DZ basis set. However, it has been noted that TD-DFT overestimates charge transfer energies,[66,67] and so several other approaches were attempted. The spectrum was calculated using the configuration interaction method CIS;[60] however, this method resulted in less satisfactory agreement with experiment, both with respect to charge transfer and $\pi\rightarrow\pi^*$ transitions. This is probably unsurprising, since this method is known to overestimate excited state energies.[68] Use of TD-DFT with long-range corrected functionals, namely, CAM-B3LYP and LC-wPBE, which has been reported to better model charge transfer transitions,[66,69] also gave unsatisfactory results. On the other hand, incorporating diffuse and polarization functionals in the LANL2DZ basis set (LANL2DZdp) for non-Fe atoms with the PBE0 functional resulted in remarkably good agreement between calculated and observed spectra, albeit with overestimated intensities (Figure 4). Agreement between calculated excitation energies and observed spectroscopic peaks was found to be good in the case of peaks composed of predominantly $\pi \rightarrow \pi^*$ transitions and overestimated, rather than underestimated, in the case of charge transfer transitions.

In the calculated spectrum of $H_2O-Fe(III)PPIX$, the Soret peak is made up of four intense excitations that involve transitions from MOs corresponding to $a_{1u}(\pi)$ and $a_{2u}(\pi)$ to $e_g(\pi^*)$ in porphine. Excitations involving these MOs have long been used to explain the B-band of porphyrins according to the Gouterman four-orbital model,[61] and indeed, transitions involving these MOs make up 99% of the Soret peak in porphine (not shown). An interesting observation is that the energy of the MOs corresponding to $a_{2u}(\pi)$ and $a_{1u}(\pi)$ are swapped around in $H_2O-Fe(III)PPIX$ relative to porphine, an observation similar to that recently made by Pinter et al. in Ga(III)PPIX, but not Zn(II)PPIX.[29] In addition, by contrast to porphine, these transitions only contribute between 14 and 37% to these excitations in $H_2O-Fe(III)PPIX$, while transitions from lower-lying π MOs make a bigger contribution to excitations in this part of the calculated spectrum. These lower-lying MOs correspond to the porphine $b_{2u}(\pi)$ and $a_{2u}'(\pi)$ MOs and are substantially delocalized onto the vinyl groups (with 18 and 11% vinyl character respectively), resulting in a loss of orbital symmetry. It is possible that this delocalization is responsible for the experimentally observed red-shift of the Soret envelope maximum of $H_2O-Fe(III)PPIX$ to 25 063 cm^{-1} (399 nm) compared to those of H_2O-Fe(III)mesoporphyrin and H_2O-Fe(III)deuteroporphyrin, in which the vinyl groups are replaced with ethyl groups and H atoms, respectively, and where the peak occurs at 25 641 cm^{-1} (390 nm) and 25 903 cm^{-1} (386 nm) respectively.[12]

Transitions corresponding to $a_{1u}/a_{2u}(\pi) \rightarrow e_g(\pi^*)$ in porphine contribute between 50 and 81% to the two excitations which underlie the calculated Q-band peak of $H_2O-Fe(III)PPIX$ at 19 608 cm^{-1} (510 nm). In the computed spectrum, the three strongest excitations underlying the peak at 17 212 cm^{-1} (581 nm) are not composed purely of charge transfer transitions but are made up of an admixture of $\pi \rightarrow \pi^*$ (corresponding to $a_{1u}/a_{2u}(\pi) \rightarrow e_g(\pi^*)$ in porphine) and $\pi \rightarrow d_\pi$ transitions, with the latter contributing between 36 and 59%. It is not immediately apparent which experimental peaks correspond to these calculated excitations, since in the absence of variable-temperature MCD we cannot make a definitive assignment. Furthermore, there is no consensus in the assignments reported for the closely related spectra of H_2O-metMb and HO-Fe(III)PPIX. In the case of the former species, Makinen and Churg assigned a peak at 18 350 cm^{-1} (545 nm) as the Q-band and peaks at 17 200 cm^{-1} (581 nm) and 15 800 cm^{-1} (633 nm) as charge transfer bands.[21] In the more recent report on HO-Fe(III)PPIX it has been suggested that the lower-energy peak at 16 722 cm^{-1} (598 nm) corresponds to the Q-band. This assignment was based on somewhat similar positions of the Q-band in Ga(III)PPIX at 17 301 cm^{-1} (578 nm) and Zn(II)PPIX at 17 153 cm^{-1} (583 nm), together with the observation of an empirical A-term shaped MCD peak.[29] The data from experimental deconvolution of the UV−visible and MCD spectra presented here tend to favor the former proposal for $H_2O-Fe(III)PPIX$, in that the envelope peak at 18 797 cm^{-1} (532 nm) appears to arise from two underlying bands corresponding to oppositely signed Gaussians in the MCD, forming a pseudo-A-term. In addition, there is an apparent Q_V-band separated by 1280 cm^{-1}. However, in contrast to the interpretation of Makinen and Churg, the lower-energy envelope would not then be purely made up of charge transfer transitions but also contain an admixture of the same $\pi \rightarrow \pi^*$ transitions seen in the Q-band. This proposed interpretation appears to be in line with chemical evidence, since the putative Q-band is relatively insensitive to the protonation state of the axial ligand, while the lower-energy envelope changes markedly upon deprotonation. This is consistent with transitions involving orbitals with substantial metal character. The suggested position of the Q-band is in agreement with the recent spectroscopic assignment of Fe(III)PPIX in cytochrome $P450_{cam}$.[28]

As noted above, recently Stillman and co-workers have reported the results of TD-DFT calculations on Zn(II)- and Ga(III)PPIX[29]. It is interesting to compare their findings to those of the $H_2O-Fe(III)PPIX$ system, especially since these authors used a different method, with B3LYP/6-31G DFT calculations being used to determine the ground-state geometries and LANL2DZ "valence + pseudopotential" used for Ga(III)PPIX TD-DFT calculations. The calculated oscillator strengths of the excitations ascribed to the Q-band fall in the same range (0.0168 and 0.0140 for Ga(III)PPIX versus 0.0429 and 0.0354 for $H_2O-Fe(III)PPIX$). In addition, there are very similar energy differences between the two highest occupied MOs (ΔHOMO) in these two molecules (0.10 eV versus 0.05 eV for Ga(III)- and Fe(III)PPIX, respectively). The HOMO−LUMO band gap calculated for Ga(III)PPIX is also very similar to that of $H_2O-Fe(III)PPIX$ (23 200 cm^{-1} versus 24 200 cm^{-1} respectively).

By comparison with $H_2O-Fe(III)PPIX$, the calculated electronic spectrum of μ-$[Fe(III)PPIX]_2O$ is vastly more complicated. This is unsurprising in view of the fact that there are almost twice the number of atoms and hence a correspondingly larger number of MOs. Although the equivalent MOs on the two porphyrins are similar, they do not possess exactly the same energies because the structure is not perfectly centrosymmetric. As a result, there are more one-electron transitions that contribute to the excited states. In addition, there is a small, but significant, number of transitions from occupied MOs predominantly localized on one porphyrin to unoccupied MOs predominantly situated on the other. These include charge transfer transitions allowed by the antiferromagnetic coupling in which both α- and β-spin MOs with metal d-orbital character are unfilled. This is in contrast to $H_2O-Fe(III)PPIX$, where only β-spin charge transfer transitions can occur. These additional factors result in many more excitations for μ-$[Fe(III)PPIX]_2O$.

It is interesting to note similarities between the computed spectroscopic properties of the μ-propionato dimer of Ga(III)-PPIX and μ-$[Fe(III)PPIX]_2O$. In the case of the former,[29] Pinter et al. note that band broadening and band doubling arises from transitions between the two rings, despite the fact that MOs are fairly localized on one ring. In addition, energies of equivalent orbitals are not identical between the two rings because they are not exactly parallel.

The calculated spectrum of antiferromagnetically coupled μ-$[Fe(III)PPIX]_2O$ displays two major peaks in the spectroscopic envelope. The Soret peak at 25 316 cm^{-1} (395 nm) consists of eight major excitations. As in $H_2O-Fe(III)PPIX$, they involve transitions corresponding to the porphine $a_{1u}/a_{2u}(\pi) \rightarrow e_g(\pi^*)$, but with larger contributions from $\pi \rightarrow \pi^*$ transitions originating in lower-lying MOs displaying substantial vinyl character. On the other hand, in comparison to H_2O−Fe(III)PPIX, there is a considerably larger charge transfer contribution to these excitations, mainly involving $\pi \to d_\pi$ transitions, but also including a small $\pi \to d_{z^2}$ component. The low-energy peak at 18 692 cm^{-1} (535 nm) differs considerably from the low-energy region of the H_2O−Fe(III)PPIX spectrum. This peak contains a number of closely spaced underlying excitations. The excitation corresponding to the Q-band (with 80% contribution from the transition corresponding to $a_{1u}/a_{2u}(\pi) \to e_g(\pi^*)$ in porphine) is very weak. Instead, the major excitations are composed of strongly configurationally mixed transitions that include this $\pi \to \pi^*$ transition as well as $\pi \to d_\pi$ transitions. There are also a number of excitations made up of predominantly $\pi \to d_{xy}$ charge transfer transitions. This spectroscopic feature of the calculated spectrum can thus neither be wholly described as a Q-band, nor a charge transfer band.

The computational study reveals certain marked differences in the MO energies of μ-$[Fe(III)PPIX]_2O$ compared with H_2O−Fe(III)PPIX. Most notably, the antibonding MOs with Fe(III) d_π and d_{z^2} character lie considerably higher in energy in μ-$[Fe(III)PPIX]_2O$. In addition, the occupied π MOs that contribute to electronic excitations are somewhat higher in energy in this species. On the other hand, the π^* MOs corresponding to $e_g(\pi^*)$ in porphine barely change in energy. As a consequence, $\pi \to d_\pi$ charge transfer transitions in the calculated spectrum occur at higher energy, while $\pi \to \pi^*$ transitions occur at lower energy. In simple terms, the Q-band can be considered to move to lower energy, where it overlaps with charge transfer bands that now arise from $\pi \to d_{xy}$ transitions. The result is a consolidated low-energy spectroscopic envelope consisting of excitations that involve both the Q-band and configurationally mixed $\pi \to \pi^*$ and charge transfer transitions. The Soret band is broadened, partly because of the shift of lower lying MOs to higher energy, thus decreasing the energy of $\pi \to \pi^*$ transitions involving these MOs. This results in a greater contribution from these transitions in the Soret region relative to H_2O−Fe(III)PPIX. In addition, excitations involving considerable $\pi \to d_\pi$ and $\pi \to d_{z^2}$ charge transfer contributions are shifted to the low-energy shoulder of the Soret band, giving rise to the prominent low-energy broadening below 24 000 cm^{-1}. The increase in energy of the Fe(III) d_π- and d_{z^2}-orbitals arises from the fact that they have considerably more porphyrin π^* character than in H_2O−Fe(III)PPIX. This probably arises as a result of increased energy of the Fe(III) d_{xz}-, d_{yz}- and d_{z^2}-orbitals owing to the weaker ligand field of O^{2-} relative to H_2O. This then results in better overlap with the porphyrin π^*-orbitals, raising the antibonding d_π MOs to higher energy. Increased doming of the porphyrin also causes improved overlap between π^*-orbitals and the Fe(III) d_{z^2}-orbital. The small increase in energy of the occupied π MOs in μ-$[Fe(III)PPIX]_2O$ probably arises as a result of increased delocalization of electron density in the dimeric species. Many of the MOs involve contributions from atomic orbitals located on both porphyrins. This energy increase results in a decrease in the energy gap between π and π^*.

A major complication in comparing the calculated spectrum of μ-$[Fe(III)PPIX]_2O$ with the experimental spectrum is that the former is treated as strictly diamagnetic, whereas the latter is paramagnetic at any temperature above 0 K. Comparison of the calculated spectra of antiferromagnetically coupled μ-$[Fe(III)P]_2O$ with its paramagnetic ($S = {}^{10}/_{2}$) counterpart shows similar composition in the Soret region. In this model compound, the Soret peak in both cases is composed of two closely spaced excitations mainly composed of $\pi \to \pi^*$ transitions, but as in the case of antiferromagnetically coupled μ-$[Fe(III)PPIX]_2O$, also with considerable $\pi \to d_\pi$ contributions. The low-energy peak shows more change in going from the antiferromagnetic to the paramagnetic state in μ-$[Fe(III)P]_2O$. In both cases, it consists of two closely spaced underlying excitations involving both $\pi \to \pi^*$ and $\pi \to d_\pi$ transitions, but in the paramagnetic species there is a substantial red shift of the main peak and it exhibits much smaller charge transfer contributions, but with an additional $\pi \to d_{z^2}$ excitation underlying this peak. In view of these findings, it seems probable that the main features of the experimental spectrum, namely, the Soret peak at 25 126 cm^{-1} (398 nm) and the low-energy envelope at 16 863 cm^{-1} (593 nm), are similarly composed. More specifically, the Soret peak likely consists of a combination of $\pi \to \pi^*$ transitions that include both the counterparts of the $a_{1u}/a_{2u}(\pi) \to e_g(\pi^*)$ transitions in porphine and transitions from lower-lying MOs with some vinyl character as well as a significant charge transfer component. The low-energy peak is probably a mixture of the counterparts of the $a_{1u}/a_{2u}(\pi) \to e_g(\pi^*)$ transitions of porphine and $\pi \to d_\pi$ transitions, with a possible $\pi \to d_{z^2}$ contribution. As such, it can probably be considered an overlapping envelope containing the Q-band as well as charge transfer bands.

The above interpretation of the UV−visible spectrum of μ-$[Fe(III)PPIX]_2O$ seems to be supported by experimental absorbance spectra of a range of 2,4-disubstituted μ-oxo Fe(III)porphyrins that have been shown to differ most markedly in the Soret region (with shifts in the peak maximum of up to 2066 cm^{-1}).[20] This is consistent with increased delocalization of electrons onto the vinyl groups encompassing MOs involved in the transitions giving rise to this peak. Furthermore, the high-energy shoulder is closest to the Soret peak maximum in μ-$[Fe(III)PPIX]_2O$, the only example reported in which the substituent is conjugated with the porphyrin. The others all exhibit a distinct high-energy peak split from the Soret peak, a feature that is reproduced in the computed spectra of both the antiferromagnetically coupled and paramagnetic forms of the unsubstituted μ-$[Fe(III)P]_2O$ molecule. Conversely, the peak of the envelope of the experimental spectrum that incorporates the Q-band, which is not predicted to involve transitions from lower-lying orbitals in μ-$[Fe(III)P]_2O$ or μ-$[Fe(III)PPIX]_2O$, is found to be largely unaffected by changes in porphyrin substituents (with shifts not exceeding 280 cm^{-1}). This insensitivity arises from the fact that the filled MOs corresponding to $a_{1u}(\pi)$, $a_{2u}(\pi)$ (HOMO and HOMO − 1), and the unfilled MO corresponding to $e_g(\pi^*)$ are hardly influenced by the presence of these substituents, an observation previously noted by others.[29]

■ CONCLUSIONS

Use of OPBE/LANL2DZ to model H_2O−Fe(III)PPIX and μ-$[Fe(III)PPIX]_2O$ produces structures and vibrational spectroscopic energies and intensities that are in good agreement with experimental data. Employment of TD-DFT with PBE0/LANL2DZ:LANL2DZdp reproduced the major features of the experimental UV−visible absorbance spectra of H_2O−Fe(III)PPIX and μ-$[Fe(III)PPIX]_2O$ remarkably well. The calculated excitations of H_2O−Fe(III)PPIX consist of configurationally mixed one-electron transitions that are generally in good agreement with previous reports. In particular, the Q-band can be largely ascribed to an excitation involving $\pi \to \pi^*$ transitions corresponding to the admixed $a_{1u}(\pi) \to e_g(\pi^*)$ and

$a_{2u}(\pi) \rightarrow e_g(\pi^*)$ reported for symmetrical D_{4h} porphyrins. The Soret peak also exhibits a major contribution from the same transitions, in agreement with the long-established Gouterman four-orbital model. However, there are notable contributions to this peak from transitions involving lower-energy occupied π-MOs. Excitations giving rise to features lower in energy than the Q-band involve transitions from lower-energy π-orbitals to d_π MOs with significant contributions from $\pi \rightarrow \pi^*$ transitions.

The interpretation of the spectrum of μ-[Fe(III)PPIX]$_2$O differs markedly from that of H_2O−Fe(III)PPIX. The main Soret peak as well as almost all of the lower energy excitations are made up of overlapping bands, some consisting of predominantly $\pi \rightarrow \pi^*$ transitions and others including significant contributions from charge transfer transitions. Indeed, the main low-energy peak cannot be thought of as either a Q-band or charge transfer band, but rather a superimposition of the two. This appears to arise as a result of the delocalization of MOs between the two porphyrins of the dimer, the decreased ligand field strength of the O^{2-} ligand relative to H_2O, and the antiferromagnetic coupling of the Fe(III) electrons, leading to both α- and β-spin charge transfer transitions. This emphasizes the fact that the major distinguishing features of the absorbance spectrum of μ-[Fe(III)PPIX]$_2$O are not accidental but rather a result of its unique electronic and structural properties. Such a spectrum must therefore be observed upon formation of this specific species. Furthermore, the marked difference between the observed MCD spectra of H_2O−Fe(III)PPIX and μ-[Fe(III)PPIX]$_2$O recommends this technique as exceptionally well suited for identifying the presence of this dimer. While the room-temperature MCD spectra reported here provide excellent fingerprint identification of these species, variable temperature/variable field MCD would be required for better identification of the underlying bands in the spectrum and their assignment to calculated excitations.

Given the ability of the DFT functionals and basis sets used in this study to reproduce both the structural and electronic properties of H_2O−Fe(III)PPIX and μ-[Fe(III)PPIX]$_2$O, these models represent a suitable starting point for accurate modeling of Fe(III)PPIX interactions with antimalarial drugs. Such studies are currently underway in our laboratories.

■ ASSOCIATED CONTENT

S Supporting Information

Experimental IR spectra of H_2O−Fe(III)PPIX and Cl−Fe(III)PPIX, details of magnetic susceptibility measurements, computed geometries of H_2O−Fe(III)PPIX obtained using M06 with LANL2DZ and 6-31G(2d,p) and M06 with LANL2DZ, structures of H_2O−Fe(III)P and μ-[Fe(III)P]$_2$O, porphinate orbital energy diagram and MOs, comparison of calculated UV−visible spectra of H_2O−Fe(III)PPIX obtained using different functionals and methods, details of band deconvolution and band-fitting parameters used in simultaneous deconvolution of UV−visible absorbance and MCD spectra, μ-[Fe(III)P]$_2$O orbital energy diagrams for both the antiferromagnetically coupled and paramagnetic forms, MOs and MO compositions, predicted spectra of these species, transitions and excitations associated with these spectra, and coordinates of geometry optimized structures of H_2O−Fe(III)PPIX and μ-[Fe(III)PPIX]$_2$O. This material is available free of charge via the Internet at http://pubs.acs.org.

■ AUTHOR INFORMATION

Corresponding Author

*Tel: +27-21-650-2528. Fax: +27-21-650-5195. E-mail. Timothy.Egan@uct.ac.za.

Notes

The authors declare no competing financial interest.

■ ACKNOWLEDGMENTS

Financial support for this work was provided by the National Research Foundation. Any opinion findings and conclusions or recommendations expressed in this material are those of the author(s) and therefore the NRF does not accept any liability in regard thereto. The University of Cape Town is also acknowledged for financial support. Part of this work is based upon research supported by the South African Research Chairs Initiative (SARChI) of the Department of Science and Technology and the National Research Foundation (NRF) awarded to K.J.N. We thank the Centre for High Performance Computing (CHPC) for use of their resources. We thank Dr. Katherine de Villiers for critically reading the manuscript.

■ REFERENCES

(1) Valerio, L. G. J. *Toxicol. Mech. Method.* **2007**, *17*, 497.

(2) Robinson, S. R.; Dang, T. N.; Dringen, R.; Bishop, G. M. *Redox Rep.* **2009**, *14*, 228.

(3) Cairo, G.; Recalcati, S.; Mantovani, A.; Locati, M. *Trends Immunol.* **2011**, *32*, 241.

(4) Krewulak, K. D.; Vogel, H. J. *Biochim. Biophys. Acta, Biomembr.* **2008**, *1778*, 1781.

(5) Braun, V.; Hantke, K. *Curr. Opin. Chem. Biol.* **2011**, *15*, 328.

(6) de Villiers, K. A.; Egan, T. J. *Molecules* **2009**, *14*, 2868.

(7) Biot, C.; Dive, D. *Top. Organomet. Chem* **2010**, *32*, 155.

(8) Carter, M. D.; Hoang, A. N.; Wright, D. W. In *Wiley Encylopedia of Chemical Biology*; Begley, T. P., Ed.; Wiley: Hoboken, NJ, 2009; Vol. 2, p 250.

(9) Brown, S. B.; Dean, T. C.; Jones, P. *Biochem. J.* **1970**, *117*, 733.

(10) de Villiers, K. A.; Kaschula, C. H.; Egan, T. J.; Marques, H. M. *J. Biol. Inorg. Chem.* **2007**, *12*, 101.

(11) Asher, C.; de Villiers, K. A.; Egan, T. J. *Inorg. Chem.* **2009**, *48*, 7994.

(12) Crespo, M. P.; Tilley, L.; Klonis, N. *J. Biol. Inorg. Chem.* **2010**, *15*, 1009.

(13) Casabianca, L. B.; An, D.; Natarajan, J. K.; Alumasa, J. N.; Roepe, P. D.; Wolf, C.; de Dios, A. C. *Inorg. Chem.* **2008**, *47*, 6077.

(14) Casabianca, L. B.; Kallgren, J. B.; Natarajan, J. K.; Alumasa, J. N.; Roepe, P. D.; Wolf, C.; de Dios, A. C. *J. Inorg. Biochem.* **2009**, *103*, 745.

(15) Brown, S. B.; Jones, P.; Lantzke, I. R. *Nature* **1969**, *223*, 960.

(16) Adams, P. A.; Berman, P. A. M.; Egan, T. J.; Marsh, P. J.; Silver, J. *J. Inorg. Biochem.* **1996**, *63*, 69.

(17) Silver, J.; Lukas, B. *Inorg. Chim. Acta* **1983**, *78*, 219.

(18) Cheng, L.; Lee, J.; Powell, D. R.; Richter-Addo, G. B. *Acta Crystallogr.* **2004**, *E60*, m1340.

(19) Brémard, C.; Kowalewski, P.; Merlin, J. C.; Moreau, S. *J. Raman Spectrosc.* **1992**, *23*, 325.

(20) O' Keeffe, D. H.; Barlow, C. H.; Smythe, G. A.; Fuchsman, W. H.; Moss, T. H.; Lilienthal, H. R.; Caughey, W. S. *Bioinorg. Chem.* **1975**, *5*, 125.

(21) Makinen, M. W.; Churg, A. K. In *Iron Porphyrins. Part I. Physical Bioinorganic Chemistry Series*; Lever, A. B. P., Gray, H. B., Eds.; Addison-Wesley: Reading, MA, 1983; p 141.

(22) Loew, G. H. In *Iron Porphyrins. Part 1*; Lever, A. B. P., Gray, H. B., Eds.; Addison-Wesley: New York, 1983; p 1.

(23) Mack, J.; Stillman, M. J.; Kobayashi, N. *Coord. Chem. Rev.* **2007**, *251*, 429.

(24) Paulat, F.; Lehnert, N. *Inorg. Chem.* **2008**, *47*, 4963.

(25) Ceulemans, A.; Oldenhof, W.; Görller-Walrand, C.; Vanquickenborne, L. G. *J. Am. Chem. Soc.* **1986**, *108*, 1155.

(26) Peralta, G. A.; Seth, M.; Ziegler, T. *Inorg. Chem.* **2007**, *46*, 9111.

(27) Hu, C.; Sulok, C. D.; Paulat, F.; Lehnert, N.; Twigg, A. I.; Hendrich, M. P.; Schulz, C. E.; Scheidt, W. R. *J. Am. Chem. Soc.* **2010**, *132*, 3737.

(28) Galinato, M. G. I.; Spolitak, T.; Ballou, D. P.; Lehnert, N. *Biochemistry* **2011**, *50*, 1053.

(29) Pinter, T. B. J.; Dodd, E. L.; Bohle, D. S.; Stillman, M. J. *Inorg. Chem.* **2012**, *51*, 3743.

(30) Mason, R. W. *A Practical Guide to Magnetic Circular Dichroism Spectroscopy*; Wiley: Hoboken, NJ, 2007.

(31) Mack, J.; Stillman, M. J. *Coord. Chem. Rev.* **2001**, *219−221*, 993.

(32) Frisch, M. J.; Trucks, G. W.; Schlegel, H. B.; Scuseria, G. E.; Robb, M. A.; Cheeseman, J. R.; Scalmani, G.; Barone, V.; Mennucci, B.; Petersson, G. A.; Nakatsuji, H.; Caricato, M.; Li, X.; Hratchian, H. P.; Izmaylov, A. F.; Bloino, J.; Zheng, G.; Sonnenberg, J. L.; Hada, M.; Ehara, M.; Toyota, K.; Fukuda, R.; Hasegawa, J.; Ishida, M.; Nakajima, T.; Honda, Y.; Kitao, O.; Nakai, H.; Vreven, T.; Montgomery, J. A. J.; Peralta, J. E.; Ogliaro, F.; Bearpark, M.; Heyd, J. J.; Brothers, E.; Kudin, K. N.; Staroverov, V. N.; Kobayashi, R.; Normand, J.; Raghavachari, K.; Rendell, A.; Burant, J. C.; Iyengar, S. S.; Tomasi, J.; Cossi, M.; Rega, N.; Millam, N. J.; Klene, M.; Knox, J. E.; Cross, J. B.; Bakken, V.; Adamo, C.; Jaramillo, J.; Gomperts, R.; Stratmann, R. E.; Yazyev, O.; Austin, A. J.; Cammi, R.; Pomelli, C.; Ochterski, J. W.; Martin, R. L.; Morokuma, K.; Zakrzewski, V. G.; Voth, G. A.; Salvador, P.; Dannenberg, J. J.; Dapprich, S.; Daniels, A. D.; Farkas, Ö.; Foresman, J. B.; Ortiz, J. V.; Cioslowski, J.; Fox, D. J. *Gaussian 09*; Gaussian Inc.: Wallington, 2009.

(33) Handy, N. C.; Cohen, A. J. *Mol. Phys.* **2001**, *99*, 403.

(34) Perdew, J. P.; Burke, K.; Ernzerhof, M. *Phys. Rev. Lett.* **1996**, *77*, 3865.

(35) Dunning, T. H. J.; Hay, P. J. In *Methods of Electronic Structure Theory*; Schaefer, H. F. I., Ed.; Plenum Press: New York, 1977; Vol. 3, p 1.

(36) Hay, P. J.; Wadt, W. R. *J. Chem. Phys.* **1985**, *82*, 270.

(37) Hay, P. J.; Wadt, W. R. *J. Chem. Phys.* **1985**, *82*, 284.

(38) Hay, P. J.; Wadt, W. R. *J. Chem. Phys.* **1985**, *82*, 299.

(39) Bacskay, G. B. *Chem. Phys.* **1981**, *61*, 385.

(40) Pagola, S.; Stephens, P. W.; Bohle, D. S.; Kosar, A. D.; Madsen, S. K. *Nature* **2000**, *404*, 307.

(41) Schaftenaar, G.; Noordik, J. H. *J. Comput.-Aided Mol. Des.* **2000**, *14*, 123.

(42) *Avogadro: An open-source molecular builder and visualization tool. Version 1.0.3*; http://avogadro.openmolecules.net/.

(43) Schmitt, E. A.; Noodleman, L.; Baerends, E. J.; Hendrickson, D. N. *J. Am. Chem. Soc.* **1992**, *114*, 6109.

(44) Marenich, A. V.; Cramer, C. J.; Truhlar, D. G. *J. Phys. Chem. B* **2009**, *113*, 6378.

(45) Adamo, C.; Barone, V. *J. Chem. Phys.* **1999**, *110*, 6158.

(46) Check, C. E.; Faust, T. O.; Bailey, J. M.; Wright, B. J.; Gilbert, T. M.; Sunderlin, L. S. *J. Phys. Chem. A* **2001**, *105*, 8111.

(47) Allouche, A.-R. *J. Comput. Chem.* **2000**, *32*, 174.

(48) Gorelsky, S. I.*SWizard program*; University of Ottawa: Ottawa, 2010; http://www.sg-chem.net/.

(49) Gorelsky, S. I.; Lever, A. B. P. *J. Organomet. Chem.* **2001**, *635*, 187.

(50) Becke, A. D. *Phys. Rev. A* **1988**, *38*, 3098.

(51) Perdew, J. P. *Phys. Rev. B* **1986**, *33*, 8822.

(52) Zhao, Y.; Truhlar, D. G. *Theor. Chem. Acc.* **2008**, *120*, 215.

(53) Pavlik, J. W.; Barabanshikov, A.; Oliver, A. G.; Alp, E. E.; Sturhan, W.; Zhao, J.; Sage, T.; Scheidt, W. R. *Angew. Chem., Int. Ed.* **2010**, *49*, 4400.

(54) Swart, M. *J. Chem. Theory Comput.* **2008**, *4*, 2057.

(55) Swart, M.; Groenhof, A. R.; Ehlers, A. W.; Lammertsma, K. *J. Phys. Chem. A* **2004**, *108*, 5479.

(56) *Cambridge Structural Database and Cambridge Structrural Database System V 1.13*; Cambridge Crystallographic Data Centre, University Chemical Laboratory: Cambridge, 2011.

(57) Cheng, B.; Safo, M. K.; Orosz, R. D.; Reed, C. A.; Debrunner, P. G.; Scheidt, W. R. *Inorg. Chem.* **1994**, *33*, 1319.

(58) Yanai, T.; Tew, D.; Handy, N. C. *Chem. Phys. Lett.* **2004**, *393*, 51.

(59) Tawada, Y.; Tsuneda, T.; Yanagisawa, S.; Yanai, T.; Hirao, K. *J. Chem. Phys.* **2004**, *120*, 8425.

(60) Foresman, J. B.; Head-Gordon, M.; Pople, J. A.; Frisch, M. J. *J. Chem. Phys.* **1992**, *96*, 135.

(61) Gouterman, M. *J. Chem. Phys.* **1959**, *30*, 1139.

(62) Platt, J. R. *J. Chem. Phys.* **1949**, *17*, 484.

(63) Moffitt, W. *J. Chem. Phys.* **1954**, *320*, 320.

(64) Mack, J.; Asano, Y.; Kobayashi, N.; Stillman, M. J. *J. Am. Chem. Soc.* **2005**, *127*, 17697.

(65) Stanek, J.; Dziedzic-Kocurek, K. *J. Magn. Magn. Mater.* **2010**, *322*, 999.

(66) Peach, M. J.; Benfield, P.; Helgaker, T.; Tozer, D. J. *J. Chem. Phys.* **2008**, *128*, 044118.

(67) Dreuw, A.; Head-Gordon, M. *J. Am. Chem. Soc.* **2004**, *126*, 4007.

(68) Mennucci, B. In *Computational Spectroscopy: Methods, Experiments and Applications*; Grunenberg, J., Ed.; Wiley: Weinheim, Germany, 2010; p 151.

(69) Le Bahers, T.; Adamo, C.; Ciofini, I. *J. Chem. Theory Comput.* **2011**, *7*, 2498.